Bioactive Materials 26 (2023) 194–215

Contents lists available at ScienceDirect

Bioactive Materials

journal homepage: www.keaipublishing.com/en/journals/bioactive-materials

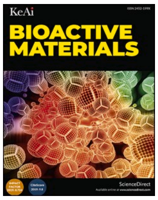

Exosomes-loaded electroconductive nerve dressing for nerve regeneration and pain relief against diabetic peripheral nerve injury

Qinfeng Yang[a,1], Shenghui Su[b,1], Shencai Liu[a,1], Sheng Yang[a], Jing Xu[c], Yixiu Zhong[d], Yusheng Yang[e], Liangjie Tian[e], Zilin Tan[f], Jian Wang[a], Zhiqiang Yu[g,h,***], Zhanjun Shi[a,**], Fangguo Liang[i,*]

[a] *Division of Orthopaedic Surgery, Department of Orthopaedics, Nanfang Hospital, Southern Medical University, Guangzhou, Guangdong, 510515, China*
[b] *Department of Orthopaedics, Ningde Municipal Hospital of Ningde Normal University, Ningde, Fujian, 352100, China*
[c] *Department of Ophthalmology, Nanfang Hospital, Southern Medical University, Guangzhou, Guangdong, 510515, China*
[d] *Department of Dermatology, Shenzhen People's Hospital (The Second Clinical Medical College, Jinan University, The First Affiliated Hospital, Southern University of Science and Technology), Shenzhen, Guangdong, 518020, China*
[e] *Division of Orthopaedics and Traumatology, Department of Orthopaedics, Nanfang Hospital, Southern Medical University, Guangzhou, Guangdong, 510515, China*
[f] *Department of General Surgery, Nanfang Hospital, Southern Medical University, Guangzhou, Guangdong, 510515, China*
[g] *Cancer Center, Integrated Hospital of Traditional Chinese Medicine, Southern Medical University, Guangzhou, Guangdong, 510515, China*
[h] *Guangdong Provincial Key Laboratory of New Drug Screening, School of Pharmaceutical Sciences, Southern Medical University, Guangzhou, Guangdong, 510515, China*
[i] *Department of Plastic and Cosmetic Surgery, Nanfang Hospital, Southern Medical University, Guangzhou, Guangdong, 510515, China*

ARTICLE INFO

Keywords:
Diabetic peripheral nerve injury
Exosomes
Electroconductive hydrogel
Nerve regeneration
Pain relief

ABSTRACT

Over the years, electroconductive hydrogels (ECHs) have been extensively applied for stimulating nerve regeneration and restoring locomotor function after peripheral nerve injury (PNI) with diabetes, given their favorable mechanical and electrical properties identical to endogenous nerve tissue. Nevertheless, PNI causes the loss of locomotor function and inflammatory pain, especially in diabetic patients. It has been established that bone marrow stem cells-derived exosomes (BMSCs-Exos) have analgesic, anti-inflammatory and tissue regeneration properties. Herein, we designed an ECH loaded with BMSCs-Exos (ECH-Exos) electroconductive nerve dressing to treat diabetic PNI to achieve functional recovery and pain relief. Given its potent adhesive and self-healing properties, this laminar dressing is convenient for the treatment of damaged nerve fibers by automatically wrapping around them to form a size-matched tube-like structure, avoiding the cumbersome implantation process. Our in vitro studies showed that ECH-Exos could facilitate the attachment and migration of Schwann cells. Meanwhile, Exos in this system could modulate M2 macrophage polarization via the NF-κB pathway, thereby attenuating inflammatory pain in diabetic PNI. Additionally, ECH-Exos enhanced myelinated axonal regeneration via the MEK/ERK pathway in vitro and in vivo, consequently ameliorating muscle denervation atrophy and further promoting functional restoration. Our findings suggest that the ECH-Exos system has huge prospects for nerve regeneration, functional restoration and pain relief in patients with diabetic PNI.

1. Introduction

Peripheral nerve injury (PNI) remains a clinical challenge, affecting more than 1 million people worldwide, reducing the quality of life of individuals and posing a huge medical and economic burden on society [1–3]. Indeed, peripheral nerve repair can be challenging in diabetic

---

Peer review under responsibility of KeAi Communications Co., Ltd.

* Corresponding author.

** Corresponding author.

*** Corresponding author. Cancer Center, Integrated Hospital of Traditional Chinese Medicine, Southern Medical University, Guangzhou, Guangdong, 510515, China.

E-mail addresses: yuzq@smu.edu.cn (Z. Yu), 18719096889@163.com (Z. Shi), 15322396396@163.com (F. Liang).

[1] These authors contributed equally to this work.

https://doi.org/10.1016/j.bioactmat.2023.02.024
Received 7 December 2022; Received in revised form 10 February 2023; Accepted 21 February 2023

patients due to persistent hyperglycemia, insulin resistance, and microvascular complications aggravating segmental axon demyelination, slow regeneration of damaged nerves, and even muscular atrophy [3–5]. The current clinical treatments for PNI include pharmacological and surgical methods (mainly decompression, neurorrhaphy and nerve grafting) [2,6–10]. Nonetheless, drugs often exhibit significant limitations for PNI repair due to their rapid degradation and redistribution in vivo and inability to promote nerve regeneration [2,3,8,9]. Accordingly, they are predominantly used for symptom management [2,3,8,9]. Additionally, surgery is associated with limitations, such as nerve decompression to avoid further injury, excessive tension induced by neurorrhaphy, limited supply as well as inevitable size or fascicle mismatch for nerve autografting, moderate re-innervation effects and low success rates of complete functional recovery after PNI [2,4,6,7,10–12]. Given the potential neuroinflammation and difficulty in repairing injured nerves, especially in diabetic patients, novel approaches are warranted to support nerve regeneration [4,13,14].

It has been established that electrical signals in the nervous system play a vital role in neural regeneration, development, remyelination and maturation [5,15–18]. In recent years, biocompatible electroconductive hydrogels with soft mechanical properties and electroconductive characteristics similar to native nerve tissue have been designed and shown great potential in promoting neuronal differentiation and axonal regrowth by providing a favorable three-dimensional (3D) biomimetic extracellular matrix (ECM) [5,15–17]. Accordingly, combining a hydrophilic matrix with electroconductive components into the extracellular microenvironment can enhance the transmission of intercellular electrical signals [5,15–17]. Most importantly, mimicking the favorable electrical transmission properties of the innate nerve tissue is of great benefit for nerve repair after PNI [5,15–17]. In previous studies, we developed several highly electroconductive, soft, adhesive, and biocompatible polymer hydrogels that could effectively facilitate neuronal and/or axonal regeneration after PNI with diabetes mellitus (DM) or spinal cord injury (SCI), thereby achieving significant recovery of locomotor function [5,15–17].

However, an increasing body of evidence suggests that PNI leads to locomotive deficits and causes persistent and unbearable pain induced by inflammation [19–21]. Notably, it is widely thought that preexisting neuroinflammation in diabetic patients may aggravate inflammatory pain after PNI [19,22]. In addition, although electroconductive hydrogels effectively promote nerve repair, their implantation into the host may result in subsequent foreign body immune reactions, which cannot relieve or even potentially exacerbate the early pain induced by acute PNI [17,23]. Therefore, the electroconductive hydrogel alone may not achieve a satisfactory effect after PNI in patients with DM. Bone marrow stem cells (BMSCs) with potent immunomodulatory properties have been applied in regulating inflammatory pain and repairing injured tissues [10,17,24–26]. BMSCs exert their anti-inflammatory effect mainly via paracrine mechanisms, among which the secretion of BMSCs-derived exosomes (Exos) act on the innate immune system via intercellular communication [17,26]. With a diameter of 30–200 nm, Exos carry various signal molecules, such as protein, lipid and miRNAs, that can be transferred into recipient cells to achieve their immunomodulatory abilities [17,27,28]. In recent years, Exos have emerged as a novel cell-free therapeutic strategy for pain relief, inflammatory diseases or damaged tissues, given their immunomodulatory and repair functions [17,26,28]. Thus, Exos-loaded electroconductive hydrogels represent a promising alternative to attenuate pain and promote functional recovery after PNI in diabetic populations.

Based on these findings, we hypothesized that an Exos-loaded electroconductive hydrogel system could synergistically yield adequate pain relief and favorable functional recovery after PNI in patients with DM. Herein, we developed BMSCs-derived Exos-loaded electroconductive hydrogel (ECH) dressings, denoted as ECH-Exos, which exhibited excellent biocompatibility, mechanical properties, conductivity, and sustained release of Exos, to achieve nerve regeneration, functional recovery, and prolonged pain relief after PNI in diabetic models. In this system, ECH was composed of tannic acid (TA) and polypyrrole (PPy), exhibiting a porous, water-rich and soft texture with adhesive and self-healing properties. Subsequently, Exos were embedded in the hydrogel network to form an ECH-Exos system through the formation of reversible interactions attributed to the existence of numerous polyphenol groups in TA. This pattern of noncovalent binding did not change the structure and biological activity of the Exos and enabled their slow and sustained release to meet the early requirement of attenuation of inflammatory pain after PNI. The micromorphological, mechanical, and electrical properties, and release of Exos from this system were validated in the present study. Next, the cell biocompatibility, adhesion, and axonal extension/migration of the PC-12 cells and/or Schwann cells (SCs) on the ECH-Exos were assessed in vitro. Finally, nerve regeneration, functional recovery and long-acting analgesia were evaluated in vivo to validate the curative effect of ECH-Exos in a diabetic sciatic nerve injury model.

2. Materials and methods

2.1. Preparation of rats BMSCs, PC-12 cells, SCs, and RAW264.7 cells

Consistent with the literature, BMSCs were acquired by repeatedly rinsing the marrow cavity of bilateral femurs and tibias of 2-week-old rats under sterile conditions [17,27,28]. Cells were collected and identified for the characterization of BMSCs (including the differentiation of adipocytes, osteoblasts, and chondrocytes by using Oil Red O staining, Alizarin Red staining and Alcian Blue staining, respectively). Low glucose Dulbecco's modified Eagle medium (DMEM, Gibco, USA) added with 10% Exos-free fetal bovine serum (FBS, Gibco, USA) and 1 × penicillin-streptomycin was utilized to culture BMSCs and the second to the sixth passage was selected for further use. PC-12 cells, SCs and RAW264.7 cells were obtained from the ATCC cell bank and cultured separately in high glucose DMEM medium (Gibco, USA) at 37 °C under 5% CO_2.

2.2. Isolation and determination of BMSCs-derived Exos

The culture medium was collected till the cells reached a confluence of 50%–60% for ultracentrifugation based on a previous study [28]. Briefly, dead cells and cell debris were removed from the supernatant after gradient centrifugation at 2000*g* for 20 min and 10,000 g for 30 min. The purified supernatant was finally centrifuged at 1×10^6 g for 90 min, and then the separated Exos were resuspended with 50 μL phosphate-buffered saline (PBS, Gibco, USA) and stored at −80 °C for further utilization. The above centrifugation procedures were performed at 4 °C. The nanoparticle tracking analysis (NTA) assay was carried out to determine the particle size of Exos. The transmission electron microscopy (TEM, JEM-1200EX, JEOL, Japan) was applied to performed the morphological observation. Western blot (WB) was carried out to detect the expression of surface markers, including Alix (ProteinTech, China), CD63 (Affinity, China) and TSG101 (ProteinTech, China) [29–33]. Exos were stained by the red fluorescent dye PKH26 (Sigma-Aldrich, USA) based on our previous protocols [17].

2.3. Fabrication of ECH

As described in our previous study, 4 mg of TA powder (Aladdin, Shanghai, China) was weighed and dissolved in 0.6 mL deionized (DI) water to prepare TA solution. Next, 35 μL (equal to 0.5 mmol) pyrrole solution (Py, 99%, Sigma-Aldrich, USA) was added into the TA solution followed by stirring to obtain solution A. Subsequently, 0.316 g of ferric chloride hexahydrate ($FeCl_3 \cdot 6H_2O$, 98%, Aladdin, Shanghai, China) was dissolved in 0.6 mL DI water for the preparation of Solution B. Finally, solutions A and B were mixed quickly at 4 °C to form a gel. The resulting hydrogels were incubated in DI water for 3 days to remove the residual reaction reagents [5,16].

2.4. Fabrication of ECH-Exos composite

Based on our prior works, 200 μg of BMSCs-Exos was dripped onto 50 μL of solution A, followed by stirring to acquire a homogeneous suspension deemed as solution C [17]. Similarly, 50 μL of solution B and solution C were mixed gently at 4 °C for gelation.

2.5. Characterization of ECH-Exos hydrogels

2.5.1. Fourier transform infrared spectroscopy (FTIR)

The functional groups and chemical composition of the hydrogels were explored by a Nicolet IS10 spectrometer (Thermo Scientific, USA) with transmission modes over 32 scans at a 4 cm^{-1} resolution. The lyophilized samples were first ground completely into powders, then pressed into pieces, and finally measured using the spectrum software.

2.5.2. Scanning electron microscopy (SEM)

The morphological observation of hydrogels was performed at an accelerating voltage of 10 kV by a SEM (ZEISS Ultra 55, Germany). The samples were lyophilized and sputter-coated with platinum (Pt) for 60 s for further scanning observation.

2.5.3. Rheological properties

Rheological experiments of the hydrogels were conducted using a rotary rheometer (Physician MCR301, Anton Paar, Austria). The angular frequency sweep (0.1–10 Hz) was performed at a fixed strain of 1%. The storage modulus (elastic modulus, G′) and loss modulus (viscous modulus, G") were respectively acquired from frequency-modulus curves.

2.5.4. Electrical properties

The electrical capability of each sample, including the cyclic voltammetry (CV) and electrochemical impedance spectroscopy (EIS), was performed using an electrochemical workstation (Zennium Zahner, Germany). A platinum counter electrode and an Ag/AgCl reference electrode were utilized in the experiments. The working electrode was prepared by hydrogels with or without Exos anchored on indium-tin-oxide (ITO) coated glass and detected in an electrolyte solution of PBS (pH = 7.4, 0.1 M). The CV measurements were conducted at a scan rate of 10 mV/s, ranging from −0.8 V to 1.0 V. EIS was conducted at frequencies from 0.01 Hz to 1×10^6 Hz and an amplitude of 5 mV utilizing the same three-electrode system.

2.5.5. In vitro exos release

Daily and cumulative release profiles were evaluated via a bicinchoninic acid (BCA) kit (Beyotime, China) based on our previous research [27,28]. 100 μL of ECH-Exos hydrogel containing 200 μg of Exos was used to assess the release profile of the Exos. Three ECH-Exos were incubated in PBS at 37 °C for 0, 1, 3, 5, 7, 10 and 14 days to explore the Exos-releasing properties. The amount of loaded Exos was calculated by subtracting the released Exos in the PBS from the total amount of Exos.

2.5.6. Phagocytosis of exos

PC-12 cells were cultured on the surface of ECH-Exos for 1 day to investigate whether Exos released from the hydrogels could be phagocyted by cells. Briefly, cells were fixed by 4% paraformaldehyde for 30 min, followed by incubation in a solution containing both 0.2% Triton-100X (Biofroxx, Germany) with membrane-breaking properties and 3% bovine serum albumin (BSA, Biofroxx, Germany) with blocking potential at 37 °C for 1 h. Afterward, β-Actin Tracker Green (Beyotime, China) was added for another 1 h. Finally, after the nucleus was stained with Hoechst 33342 (Sigma, USA) for 5 min, images were obtained by a laser confocal microscope (ZEISS LSM 980, Germany).

2.6. In vitro studies

2.6.1. Cell viability and biocompatibility assessment

The live/dead assay, cell counting kit-8 (CCK-8, Dojindo, Japan), and cytoskeletal staining were applied to evaluate the in vitro biocompatibility of samples. To perform the live/dead staining test, PC-12 cells and SCs with a density of 5×10^5 were separately seeded on each sample for 24 h. Next, the live/dead solution containing calcein-AM (Invitrogen, USA), propidium iodide (PI, Invitrogen, USA) and PBS was prepared and then added to each sample for 30 min at 37 °C, followed by observing under a laser confocal microscope (ZEISS LSM 980, Germany). The proliferation of PC-12 cells and SCs was assessed by CCK-8 assay (Beyotime, China) after 5×10^5 cells were co-incubated with each sample for 1, 3, and 7 days. CCK-8 solution at a concentration of 100 μL/mL was added into 12-well plates and incubated for 2 h. Subsequently, 100 μL supernatant was added into a 96-well plate, and the optical density (OD) or absorbance was measured at 450 nm wavelength using an enzyme labeling instrument (BioTech, Germany). The calculation of cell viability was the ratio of OD value between the experimental and control groups. The cytoskeletal staining of PC-12 cells and SCs was conducted as follows. In brief, cells with a density of 1×10^5 were cultured on each sample in 12-well plates for 3 days, then fixed with 4% paraformaldehyde, followed by staining with β-Actin Tracker Green (Beyotime, China) and Hoechst (Sigma, USA), and finally observed under a laser confocal microscope (ZEISS LSM 980, Germany).

2.6.2. Cell migration assay

For the cell migration assay, a transverse scratch was created to simulate an artificial wound after the SCs reached a confluence of about 90%. Next, PBS was used to wash the samples thrice gently to remove the floating cells and stained using calcein AM (Invitrogen, USA) after culturing for 12 h and 24 h. Then, the micrographs were acquired with a confocal microscope (ZEISS LSM 980, Germany).

2.6.3. Gene expression

The total RNA was harvested using a total RNA kit (Omega, USA) and then reverse-transcribed into cDNA by a reverse transcription kit (Takara, Japan). Real-time qPCR (RT-qPCR) was conducted using the LightCycler 480 SYBR Green Master Mix (Takara, Japan). This experiment was repeated in triplicates followed by calculating with the $2^{-\Delta\Delta Ct}$ method. Table 1 displayed the primers used in the present study.

2.6.4. Immunofluorescence (IF)

4% paraformaldehyde was used to fix cells or tissues for 30 min. Next, these fixed samples were permeabilized by 0.2% Triton X-100 (Biofroxx, Germany) for 1 h at room temperature, followed by blocking with 3% BSA (Biofroxx, Germany) for 1 h. Then, they were incubated in corresponding primary antibodies overnight at 4 °C (Table 2). After the samples were washed thrice with PBS, secondary antibodies were added for another 1 h at room temperature. Ultimately, Hoechst 33342 (Sigma, USA) was used to stain the nuclei before the fluorescent images were visualized under a confocal reflection microscope (ZEISS LSM 980, Germany).

2.6.5. WB assay

Cells or tissues were washed with PBS and dissolved in radioimmunoprecipitation assay (RIPA, CWBIO, China) buffer with the addition of protease and phosphatase inhibitors (Thermo Fisher, USA). Next, the suspensions were lysed further by ultrasound followed by centrifuging at 4 °C. The obtained supernatant was transferred to a new centrifuge and preserved at −20 °C. The measurement of total protein concentration was completed with a BCA assay kit (Beyotime, China). After the supplement of loading buffer (Beyotime, China) to protein supernatant and denaturation under the condition of 100 °C for 10 min, equal amounts (40 μg) of protein suspension were loaded on sodium dodecyl sulfate-polyacrylamide gel electrophoresis (SDS-PAGE,

Table 1
Primer sequences of each gene.

Target	Forward	Reverse
GAPDH	AGACAGCCGCATCTTCTTGT	CTTGCCGTGGGTAGAGTCAT
NF	GTTCCGAGTGAGGTTGGACC	CCGCCGGTACTCAGTTATCTC
GAP43	GCACATCGGCTTGTTTAGGCT	GGAGGGAGATGGCTCTGCTACT
TUJ1	CCCGTTTTAGCCACCTTTGTATT	CCCTCCAAATATAAACACAACCC
SYN	CTTCCTGGTTGGGGACTACTCCTC	GCGAACACGGCTGTAGCCAGAAAG
Arg-1	CTCCAAGCCAAAGTCCTTAGAG	GGAGCTGTCATTAGGGACATCA
IL-10	CTTACTGACTGGCATGAGGATCA	GCAGCTCTAGGAGCATGTGG
iNOS	GTTCTCAGCCCAACAATACAAGA	GTGGACGGGTCGATGTCAC
TNF-α	CGAGTGACAAGCCTGTAGCC	ACAAGGTACAACCCATCGGC

Table 2
Related information about primary antibodies.

Antibodies	Species	Type	Dilution (IF/WB)	Source
Anti-GAPDH	Rabbit	Monoclonal lgG	1:1000	CST, America
Anti-Neurofilament (NF)	Rabbit	Polyclonal lgG	1:200/ 1:1000	ProteinTech, China
Anti-Growth-associated protein-43 (GAP43)	Rabbit	Polyclonal lgG	1:2000	ProteinTech, China
Anti-Myelin basic protein (MBP)	Rabbit	Polyclonal lgG	1:2000	ProteinTech, China
Anti-S100 beta (S100)	Rabbit	Polyclonal lgG	1:1000	ProteinTech, China
Anti-Arg-1	Rabbit	Polyclonal lgG	1:1000	GeneTex, America
Anti-iNOS	Rabbit	Polyclonal lgG	1:1000	GeneTex, America
Anti-MEK1/2	Mouse	Monoclonal lgG	1:1000	CST, America
Anti-Phospho-MEK1/2 (Ser217/221)	Rabbit	Monoclonal lgG	1:1000	CST, America
Anti-p44/42 MAPK (Erk1/2)	Rabbit	Monoclonal lgG	1:1000	CST, America
Anti-Phospho-MAPK (Erk1/2) (Thr202/ Tyr204)	Rabbit	Monoclonal lgG	1:1000	CST, America
Anti-IKBα	Mouse	Monoclonal lgG	1:1000	CST, America
Anti-p-IKBα	Rabbit	Monoclonal lgG	1:1000	CST, America
Anti-P65	Rabbit	Monoclonal lgG	1:1000	CST, America
Anti-p-P65	Rabbit	Monoclonal lgG	1:1000	CST, America
Anti-Alix	Rabbit	Polyclonal lgG	1:2000	ProteinTech, China
Anti-CD63	Rabbit	Polyclonal lgG	1:1000	Affinity, China
Anti-TSG101	Mouse	Monoclonal lgG	1:5000	ProteinTech, China

Beyotime, China) to separate proteins. Afterward, proteins were transferred onto polyvinylidene difluoride (PVDF, Thermo Fisher, USA) membranes. The PVDF membranes were then blocked with high-efficiency blocking solution (Genefist, China) for 10 min followed by incubating with the specific primary antibodies (Table 2) at 4 °C overnight. After incubation with corresponding secondary antibodies, the protein bands were visualized with an enhanced chemiluminescence (ECL, Thermo Fisher, USA) kit and the images were acquired using the GelView 6000 Pro (BLT, China). Finally, the density of bands was quantitatively analyzed by ImageJ software.

2.7. *In vivo studies*

2.7.1. *Ethical statement*

All animal experiments were performed after the approvement of the Animal Experimental Ethics Committee of Nanfang Hospital of Southern Medical University and complied with the requirements of the National Institutes of Health Guide for the Care and Use of Laboratory Animals.

2.7.2. *Diabetic sciatic nerve crush injury*

Adult female Sprague-Dawley (SD) rats (300-350 g) supplied by the Southern Medical University Laboratory Animal Center (Guangzhou, China) were used in this study. As previously described, streptozotocin (STZ) buffer was intraperitoneally injected into rats at 70 mg/kg to establish a diabetic model [5]. A random concentration of blood glucose above 16.7 mmol/L confirmed the occurrence of DM based on established guidelines [5,34]. 36 diabetic rats were selected and randomly assigned into four groups (PNI, ECH, Exos, and ECH-Exos, n = 9 per group). The weight and blood glucose values of the animals are shown in Fig. S1.

Diabetic animals were first anesthetized by intraperitoneal injection of pentobarbital (50 mg/kg). The diabetic sciatic nerve crush injury model was established according to prior descriptions [4,5,35,36]. After a 15-mm skin incision was made on the lateral side of the left thigh, the gluteal muscle was bluntly dissectd to expose the sciatic nerve. The sciatic nerve was crushed utilizing a pair of vascular forceps with about 30 g force and lasting for 2 min within 5 mm of the sciatic notch to create a crush injury model. The PNI group only underwent sciatic nerve crush injury and was not implanted with any foreign material. In the ECH group and ECH-Exos group, ECH dressings and ECH-Exos dressings were implanted around the damaged sciatic nerve to form tube-like structures, respectively. The Exos group received an injection of 200 μg Exos with a 25-gauge needle around the damaged sciatic nerve. Both the muscle and skin layer were closed sequentially with interrupted 4-0 vicryl stitches. The right posterior limb served as an untreated control. After the surgery, the animals were housed in warm environment and well-fed.

2.7.3. *Mechanical allodynia assay with von-Frey filaments*

According to prior protocols, a rat was separately positioned on a wire mesh floor in an individual plastic chamber and allowed to acclimate the surroundings for around 30 min before testing [37–40]. The evaluation of mechanical allodynia was conducted by the measurement of paw withdrawal threshold (PWT) via nine von-Frey filaments of ascending forces (4, 6, 8, 10, 15, 26, 60, 100, and 180 g). The force required to trigger the withdrawal, licking or biting of the hind paw was regarded as the threshold for positive responses. Stimulations were repeated 5 times per rat with a 1-min interval. The average value of these 5 readings served as an individual threshold. Tests were conducted before (4 h) and after surgery (1, 2, 3, 4, 5, 6, 7, 10, 12, and 14 d). Increased PWT suggested a decrease in mechanical allodynia or pain relief. A schematic diagram depicting this assay is exhibited in Fig. 5A.

2.7.4. *Analysis of thermal hyperalgesia response by hot plate assay*

As previously reported, a modified hot plate assay was utilized to assess thermal hyperalgesia [36,38]. In brief, an animal was positioned on a thermally conductive floor in separated plastic chamber, and the hind paws were exposed to a hot plate preheated to 56 °C. The time taken for the rats to lick or raise their hind paws was recorded as thermal withdrawal latency (TWL). The rats were habituated two days before the surgery to assess and determine the baseline TWL. Before the operation (2 h) and post-operation at predefined time points (1, 2, 3, 4, 5, 6, 7, 10, 12, and 14 d), measurements were performed. The measurements conducted right before the surgery (2 h) were considered as the baseline value of TWL. TWL measurements were repeated 5 times for each rat at each time point, and then the average value was calculated. A 1-min interval was adopted between the measurements to avoid tissue damage. Similarly, an increased TWL suggested a reduction in thermal hyperalgesia or pain relief. A schematic diagram depicting this test is exhibited in Fig. 5D.

2.7.5. Functional analysis

The walking track analysis was performed to evaluate the restoration of locomotor function at 2, 3, and 4 weeks after operation. The animals were allowed to walk through a narrow track with their hind paws coated in non-toxic blue ink. The calculation of sciatic function index (SFI) was based on three measurable footprint measurements, including print length (PL, length from the heel to the third toe), toe spread (TS, length from the first to the fifth toe), and intermediate toe spread (ITS, length from the second to the fourth toe). A schematic diagram illustrating the three footprint parameters is presented in Fig. 6E. The SFI was calculated according to the following equation (1):

$$\mathrm{SFI} = -38.3 \times \frac{(\mathrm{P}L_{\mathrm{Exp}} - \mathrm{P}L_{\mathrm{Ctrl}})}{\mathrm{P}L_{\mathrm{Ctrl}}} + 109.5 \times \frac{(\mathrm{T}S_{\mathrm{Exp}} - \mathrm{T}S_{\mathrm{Ctrl}})}{\mathrm{T}S_{\mathrm{Ctrl}}} + 13.3 \times \frac{(\mathrm{IT}S_{\mathrm{Exp}} - \mathrm{IT}S_{\mathrm{Ctrl}})}{\mathrm{IT}S_{\mathrm{Ctrl}}} - 8.8 \tag{1}$$

where Exp and Ctrl represent the experimental and normal sides, respectively.

2.7.6. Hemocompatibility and in vivo biocompatibility

Whole rat blood was collected and co-incubated with each sample at 37 °C for 4 h. PBS and Triton-100X were added and served as negative and positive groups, respectively. After centrifugation at 10,000 g for 5 min at 4 °C, the supernatant was transferred into a 96-well plate for the measurement of the absorbance at 540 nm using an enzyme-labeling instrument (BioTech, Germany). The calculation of hemolysis percentage was accomplished by the following formula (2):

$$\text{Hemolysis } (\%) = \frac{\mathrm{OD}_{\mathrm{Sample}} - \mathrm{OD}_{\mathrm{PBS}}}{\mathrm{OD}_{\mathrm{Triton}} - \mathrm{OD}_{\mathrm{PBS}}} \times 100\% \tag{2}$$

where OD represents the optical density.

Additionally, whole rat blood was collected 4 weeks after the surgery to evaluate the in vivo biocompatibility by measuring three common biochemical indicators including alanine aminotransferase (ALT), aspartate aminotransferase (AST) and total protein (TP) with an automatic biochemical analyzer (Yingnuo, Nanjing, China). Major organs, including the heart, liver, spleen, lung, and kidneys, were harvested, followed by staining with hematoxylin-eosin (HE) for pathological analysis.

2.7.7. Histological assessment of muscle and nerve fibers

4 weeks after the procedure, rats were deeply anesthetized by pentobarbital (100 mg/kg) before being sacrificed. Regenerated nerve tissues and gastrocnemius muscles were dissected and then fixed in 4% paraformaldehyde for 1 day before embedding in paraffin. To observe nerve morphology, longitudinal paraffin nerve-embedded tissue was cut into 10 μm-thick sections and stained with HE and Masson trichrome staining (MTS). To observe the morphological alterations of the ipsilateral gastrocnemius muscle, 30 μm cross-sections were stained by HE and MTS before observing under a light microscope.

2.7.8. Toluidine blue staining (TBS) and TEM

The central areas of the regenerated nerves were acquired 4 weeks after experimental procedure. The samples were dewaxed, embedded in epoxy resin, and then cut into 1 μm semi-thin cross-sections and 50 nm ultrathin cross-sections. The semi-thin sections were stained by TBS, while the ultrathin sections were prepared for TEM (JEOL, Tokyo, Japan). Morphological assessment of the myelinated axons was performed by obtaining five random images of each tissue.

2.8. Statistical analysis

SPSS version 23 (IBM, USA) and GraphPad Prism 5 and 8 software (GraphPad Software, USA) were used for statistical analyses. Groups were compared using the Kruskal-Wallis test (nonparametric data) or one-way analysis of variance (ANOVA) with Bonferroni's post-hoc test (for normally distributed data). All quantitative data were expressed as mean ± standard deviation (Mean ± SD). A *P*-value less than 0.05 was statistically significant.

3. Results and discussion

3.1. Characterization of BMSCs-Exos

The process of BMSCs-Exos isolation is briefly exhibited in Fig. 1A. To identify the isolation of Exos obtained from BMSCs, TEM images were captured and showed that the morphology of spherical vesicle was similar to a cup (Fig. 1B). NTA exhibited that the average size of these spherical vesicles was approximately 171.3 ± 100.3 nm, consistent with the above TEM results (Fig. 1C). WB analysis showed significantly higher expression of surface markers on the acquired vesicles than BMSCs, which included Alix, CD63, and TSG101 proteins (Fig. 1D) [29–33]. Taken together, these findings demonstrated the successful extraction of Exos from BMSCs.

3.2. Synthesis and characterization of ECH-Exos

Fig. 1A is a schematic diagram illustrating the process of material preparation and simple chemical structure of the ECH-Exos. The formation of ECH was a method of instant gelation within 2 s as a result of the crosslinking of PPy and TA with an addition of an oxidative initiator ($FeCl_3$). TA was crosslinked with PPy chains via intermolecular electrostatic interactions between the phenol hydroxy groups on TA and the protonated nitrogen groups on PPy. Additionally, TA is a widely acknowledged dopant since the protonation of the nitrogen groups confers electroconductive properties to PPy [5,16]. Notably, excessive Fe^{3+} ions play a critical role in the process of gelation as these Fe^{3+} ions facilitate the polymerization of Py by oxidation reaction and further form ionically crosslinked networks with TA by acting as ionic crosslinkers [5,16]. Ultimately, the BMSCs-Exos were embedded into the ECH network for the formation an ECH-Exos system via the formation of reversible bonds between the phosphate groups provided by the phospholipid surface of Exos and the numerous polyphenol groups in TA [17].

It is widely acknowledged that the mechanical properties of the extracellular matrix microenvironment can influence cell differentiation and function [5,15,16]. Consequently, the mechanical properties of ECH with or without Exos were investigated by dynamic oscillatory frequency sweep measurements. The storage moduli (elastic modulus G′) of both hydrogels were larger compared to the moduli (viscous modulus G") within an angular frequency range of 0.1–10 Hz (Fig. 1E), implying that these two hydrogels possess favorable stability and viscoelasticity. Besides, the average elastic moduli of ECH and ECH-Exos were 899 ± 66 Pa and 816 ± 75 Pa, respectively (Fig. 1F), which indicated that the immobilization of Exos barely influenced the mechanical properties of ECH. These findings illustrate that the mechanical properties of both ECH and ECH-Exos are similar to nervous system tissue (100–3000 Pa),

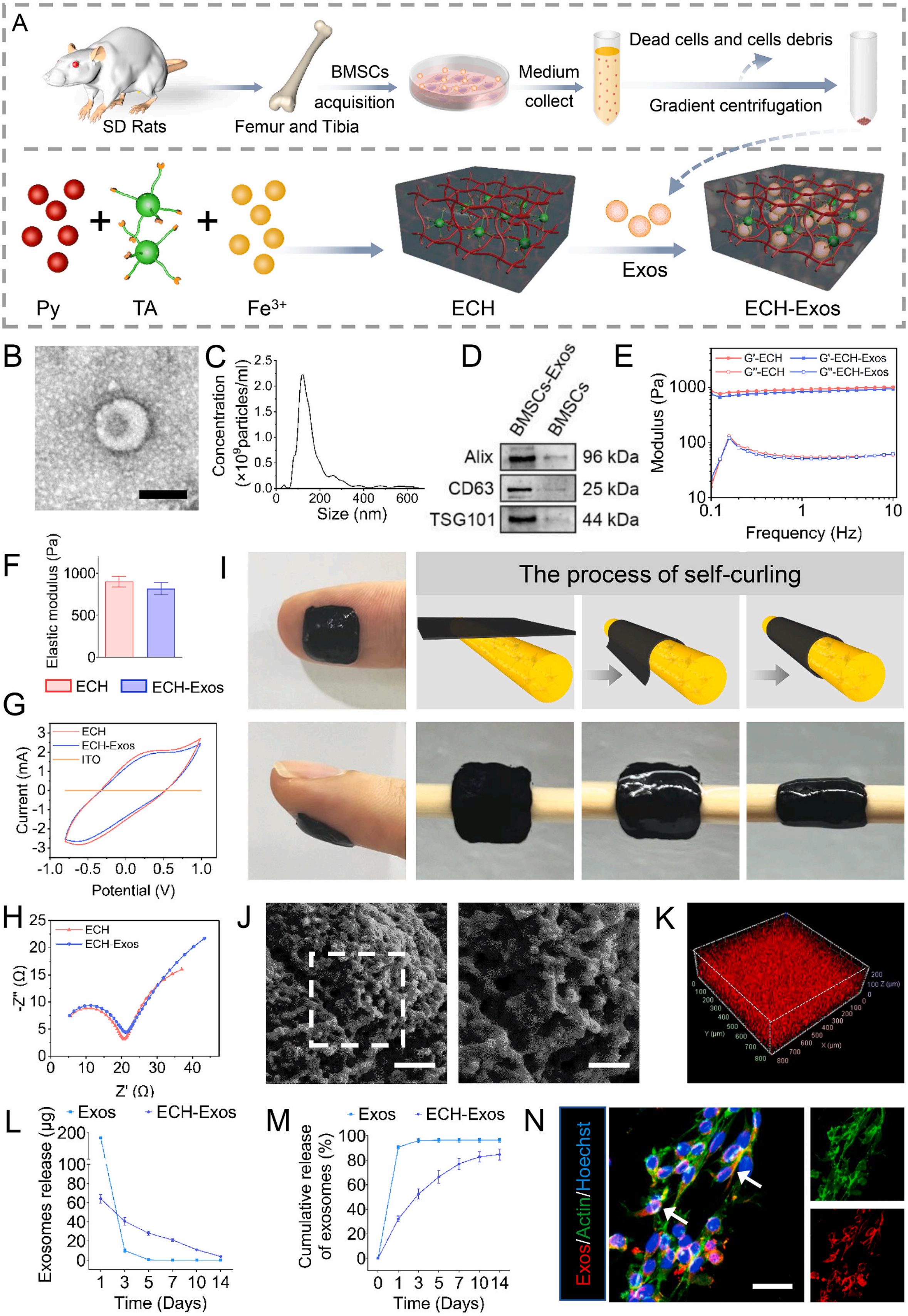

(caption on next page)

Fig. 1. Characterization of the ECH-Exos system. (A) Illustration of the synthesis and structure of the ECH-Exos system. (B) Morphology of obtained nanoparticles detected by TEM. The scale bar represents 100 nm. (C) The range of nanoparticle size was measured by NTA. (D) BMSCs-Exos surface-specific proteins, including Alix, CD63, and TSG101, were assessed by WB. (E) Rheological properties of ECH with or without Exos. (F) Graph of the quantification of mechanical properties of ECH and ECH-Exos (n = 5). (G) Cyclic voltammograms of ECH with or without Exos. (H) Nyquist curves of ECH with or without Exos. (I) Photographs and illustrations displayed adhesive and self-curling ECH-Exos as a thin film dressing that adhered to the finger and automatically wraps to form a size-matched tube-like structure. (J) The microstructure of the ECH-Exos was observed by SEM. Scale bar respectively represents 1 μm and 0.5 μm. (K) 3D IF image presented that Exos labeled with PKH26 were evenly distributed in ECH, and the penetration depth of the Exos was approximately 200 μm. (L) The daily release profile of Exos with or without ECH until day 14 (n = 3). (M) The cumulative release curve of Exos with or without ECH until day 14 (n = 3). (N) PKH26-labeled Exos were observed in the cytoplasm of PC-12 cells, indicating the successful in vitro endocytosis of Exos released from the ECH. White arrows denote where PC-12 cells have phagocytosed Exos. Scale bars represent 25 μm. Statistical differences were determined by using One-way ANOVA with Bonferroni's multiple comparison test.

providing excellent mechanical support and flexibility for axon growth [5,15–17].

Our previous studies demonstrated that electroconductive hydrogels were beneficial for PNI or SCI repair by enhancing the transmission of native bioelectrical signals [5,15–17]. Thus, the electronic properties of ECH with or without Exos were examined by an electrochemical workstation. A negligible current appeared in the ITO bare electrode exhibited, whereas the enhanced anodic and cathodic currents were observed in the ECH and ECH-Exos, attributed to the electroconductive properties of PPy (Fig. 1G). Additionally, ECH and ECH-Exos exhibited highly consistent current responses for both oxidation and reduction, indicating that the embedment of Exos did not affect the doping levels and crosslinking density, thereby exhibiting similar electrical conductivity (Fig. 1G). EIS analyses were also conducted to assess the conductivities of two hydrogels. A quasi-semicircle was seen in the high-frequency region for both ECH and ECH-Exos in the Nyquist plots, suggesting that they had great redox activity (Fig. 1H). Moreover, the diameter of the semicircle of these two hydrogels was comparable, which implied that the addition of Exos did not alter the charge-transfer resistance. These findings were consistent with the above CV results (Fig. 1H). It is well-established that the diameter of the semicircle corresponds to the charge-transfer resistance. That is, the larger diameter of the semicircle represents larger charge-transfer resistance. We found that these two hydrogels had slightly smaller semicircle diameters than our previous findings, which indicated a difference in charge-transfer resistance [5,15–17]. It is widely acknowledged that low resistance and desirable electroconductive properties are of great benifit for rapid intercellular communication via endogenic bioelectrical signals generated by the pumps or ion channels between adjacent cells [5,15–17].

Interestingly, the ECH-Exos hydrogel could adhere to irregular objects like fingers and chopsticks (Fig. 1I). This tissue adhesion property of ECH-Exos can be harnessed as a dressing to plaster nerve tissue, followed by twisting into a size-matched tube-like structure, which simplifies the troublesome implantation process of traditional biomaterials, specifically for in vivo application in diabetic patients. Indeed, damaged nerves require scaffolds to be sutured with residual nerve fibers for effective fixation [5,9,41]. Additionally, the hydrophilic properties and porous surface of the ECH-Exos are beneficial for excellent adhesion to the innate nerve tissue [5]. Moreover, the reversibility of the dopant and coordination bonds confer the hydrogel contacting with each other via end to end and instantly rebuilding an integral wrap tubular structure during the self-curling process [5]. Notably, this size-matched wrap structure allows the ECH-Exos to retain its desirable apposition with the native nerve tissue [5].

The results of FTIR spectra analysis of ECH were consistent with PPy, implying that PPy is the primary component of this hydrogel (Fig. S2). In the ECH spectrum, the characteristic stretching vibrations of the $C{=}N^{+}{-}C$ bonds and $C–N^{+}$ bonds were observed at 903 cm^{-1} and 1174 cm^{-1}, respectively, substantiating a highly doped state in the conductive hydrogel (Fig. S2) [5,16]. SEM image showed that ECH-Exos hydrogels displayed a 3D highly porous network (Fig. 1J). Besides, high-magnification SEM presented interconnected spherical nanostructures on the surface of the ECH where the Exos were successfully anchored (Fig. 1J). These porous microstructures provided favorable space for nerve cell extension and substance exchange [5,16,17]. Notably, the SEM image of ECH without Exos exhibited highly similar surface with ECH-Exos (Fig. S3), due to that both the PPy and Exos possess nanoscale spherical structures [17]. Therefore, to visualize Exos loaded on ECH, Exos were labeled with PKH26 dyes followed by visualizing under a confocal reflection microscopy. The 3D IF assay exhibited that the Exos were evenly and spatially distributed on the surface of the ECH, revealing the successful loading of BMSC-Exos (Fig. 1K). Furthermore, the in vitro Exos release from the ECH was determined for 14 days. As shown in Fig. 1L and M, approximately 80% of the loaded Exos were released from the ECH dressing until the final day, allowing Exos to exert their anti-inflammatory and repair effects during early PNI [17]. This sustained release ability of ECH may be attributed to the formation of reversible hydrogen bonds between TA and Exos [17]. Additionally, PKH26-labeled Exos were observed in the cytoplasm of PC-12 cells, implying that Exos released from the ECH-Exos could be successfully endocytosed into target cells (Fig. 1N).

3.3. *PC-12 cells viability, adhesion and axonal outgrowth on the ECH-Exos system*

The live/dead assay, CCK-8 assay, cytoskeletal staining, gene expression analysis, IF and WB assays were conducted to examine the biocompatibility and ability of the ECH-Exos hydrogel for neural regeneration by culturing PC-12 cells on slide (control) and materials. Few dead cells (red) and numerous viable cells (green) were detected in each group (Fig. 2A and B). In line with the live/dead staining, the CCK-8 results demonstrated that the proliferation of PC-12 cells cultured on each sample surpassed 80% at 1, 3, and 7 days, which confirmed that all samples were considerably biocompatible (Fig. 2C). Subsequently, cells were co-cultured with each sample 3 days before cytoskeleton staining was conducted. The synaptic length and extending area of the PC-12 cells on the ECH-Exos were significantly greater than the other groups (Fig. 2D and E). Furthermore, the relative expression of the axon growth-related genes, including neurofilaments (NF), growth-associated protein-43 (GAP43), β3-tubulin (TUJ1) and synuclein (SYN), was used to assess the capacity of ECH-Exos to support axonal outgrowth. As observed from the histogram and heat map, the relative expressions of the four genes were the highest in the ECH-Exos group (Fig. 2F and G). Besides, the neural length was observed in PC-12 cells after 3 days of culture on the ECH-Exos hydrogel (Fig. 2H). In this respect, neural activity and length in the ECH-Exos group were the highest, with a neural length of 52.55 ± 1.53 μm, which was significantly longer than in the Exos (36.73 ± 0.94 μm), ECH (45.98 ± 1.63 μm), and control (28.08 ± 1.24 μm) groups (Fig. 2I). Consistently, WB analysis substantiated that the protein levels of the postsynaptic markers including NF and GAP43 in the ECH-Exos group were significantly higher compared with the other groups (Fig. 2J and K). In addition, the genes and proteins levels in the ECH group were significantly higher than in the Exos group. Moreover, significantly higher levels were observed in the Exos group compared to the control group (Fig. 2F, G, H, I, J, K). These findings are in accordance with prior reports that the conductivity of PPy in ECH could promote neuron proliferation, activity, and neurite outgrowth by promoting intercelluar communication by bioelectric signals [10,16,42]. Furthermore, BMSCs-Exos could facilitate axonal growth due to their high expression levels of axonal regeneration-related miRNAs [17].

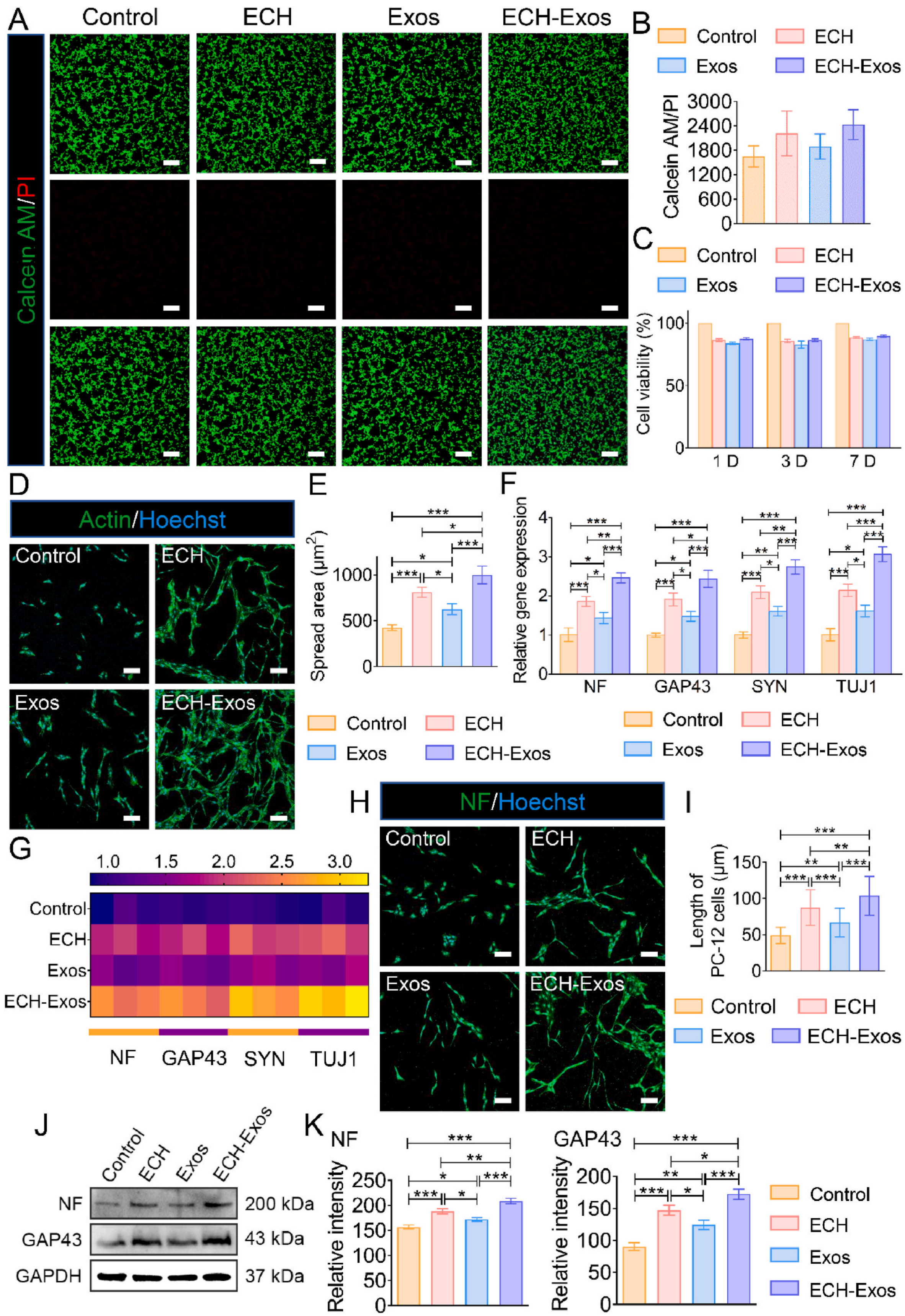

(caption on next page)

Fig. 2. PC-12 cells viability, adhesion and axonal outgrowth on the ECH-Exos. (A) Live/dead assay of the PC-12 cells cultured on each sample surface for 1 day. Live cells were stained in green and dead cells in red. The scale bar represents 200 μm. (B) Quantitative analysis of live/dead assay (n = 3). (C) The CCK-8 assay demonstrates that the cell viability surpassed 80% for each sample after seeding for 1, 3 and 7 days (n = 5). (D) The cytoskeleton images showed the adhesion of PC-12 cells cultured in each group after 3 days. The scale bar represents 100 μm. (E) Quantitative analysis of the cell spreading area (n = 9). (F) Column graph showing the RT-qPCR results on the axon-related gene expressions in PC-12 cells (n = 3). (G) The heat map depicting the RT-qPCR results on the axon-related gene expressions of the PC-12 cells (n = 3). (H) IF images for the NF (green) and cell nuclei (blue) to examine the axonal extension of the PC-12 cells. The scale bar represents 100 μm. (I) Quantitative analysis of the axonal lengths of the PC-12 cells on each sample (n = 9). (J) WB analysis was used to detect the protein expressions of NF and GAP43 in PC-12 cells cultured on each sample for 3 days. (K) Quantitative analysis of protein expression (n = 3). Statistical differences were determined by using One-way ANOVA with Bonferroni's multiple comparison test ($*P < 0.05$, $**P < 0.01$, and $***P < 0.001$).

Therefore, the combination of ECH and Exos yields a synergistic effect, especially in promoting nerve outgrowth, highlighting its huge prospects for PNI repair.

3.4. SCs viability, adhesion and migration on the ECH-Exos system

Growing evidence suggests that SCs support the metabolism of the regenerated axons, influencing the process of myelination and the formation of nodal domains, and are the primary glia in the peripheral nervous system [5,10,43]. Herein, SCs viability, proliferation, adhesion, and migration experiments were carried out to investigate the myelination of samples. Consistent with the PC-12 cells results, the live/dead assay and CCK-8 assay confirmed that the ECH-Exos hydrogel exhibited excellent biocompatibility for SCs (Fig. 3A, B, C). Cytoskeleton imaging showed that SCs cultured on the ECH-Exos hydrogel stretched better than the control, ECH and Exos groups, implying that the ECH-Exos hydrogel possessed great affinity and adhesion for SCs (Fig. 3D and E). During the wound healing assay, many SCs were distributed on the edges and into the bare site after 12 h and 24 h on the ECH-Exos hydrogel (Fig. 3F). Notably, SCs tended to cluster at the wound site in the ECH-Exos group, and were distributed randomly and intricately in the other groups (Fig. 3F). In addition, the wound area of the ECH-Exos group was significantly lower compared with the control, ECH and Exos groups after being cultured for 12 h and 24 h (Fig. 3G). The above results revealed that the ECH-Exos scaffold was suitable for cell growth, proliferation, attachment and migration, probably due to that the hydrophilic and electroconductive properties of ECHc, and Exos could synergistically promote the motility of SCs [5,17,42].

3.5. The anti-inflammatory effect of ECH-Exos

Given that macrophages are reportedly recruited to the lesion site to induce neuroinflammation and further cause inflammatory pain after PNI with diabetes, RAW264.7 cells were cultured on the ECH-Exos for 3 days to investigate whether the ECH-Exos yields an anti-inflammatory effect [19,22,27]. As shown in Fig. 4A, macrophages could be activated into the pro-inflammatory M1 and anti-inflammatory M2 phenotypes [17,24,27,44]. Exos released from ECH-Exos can be endocytosed by RAW264.7 cells to exert their immunomodulatory ability (Fig. S4). The M1 phenotype is characterized by increased expression of pro-inflammatory markers, such as inducible nitric oxide synthase (iNOS) and tumor necrosis factor-alpha (TNF-a), whereas the M2 phenotype secretes anti-inflammatory markers like arginase-1 (Arg-1) and IL-10 [17,24,27,44]. Before each experiment, lipopolysaccharide (LPS) was supplemented in medium for RAW264.7 cells to induce inflammation. RT-qPCR revealed that gene levels of the anti-inflammatory cytokines, including Arg-1 and IL-10 in RAW264.7 cells co-cultured with the ECH-Exos system, were significantly higher than in cells co-cultured with the other samples. In contrast, the mRNA expressions of the pro-inflammatory markers, including iNOS and TNF-α, were significantly lower in the ECH-Exos group than in the other three groups (Fig. 4B and C). Furthermore, the IF images exhibited that the abundance of Arg-1 positive cells was significantly higher in the ECH-Exos group than in the other groups, while the amount of iNOS positive cells was significantly lower (Fig. 4D and E). In line with the qPCR and IF findings, WB analysis verified that ECH-Exos system significantly promoted the expression of Arg-1 protein but inhibited iNOS protein levels (Fig. 4F and G). Notably, the levels of anti-inflammatory cytokines in the ECH group were slightly lower than in the control group, while the levels of pro-inflammatory cytokines were slightly higher, despite there was no significant difference (Fig. 4B, C, D, E, F, G). Moreover, treatment with Exos alone elevated the levels of anti-inflammatory cytokines and reduced the expressions of pro-inflammatory markers (Fig. 4B, C, D, E, F, G). Taken together, the above results demonstrated that the ECH hydrogel, as an exogenous implant, may induce a detrimental host inflammatory response to some extent [17,27]. Importantly, with the addition and sustained release of Exos, the ECH-Exos hydrogel confers a desirable inflammatory effect by promoting M2 macrophage polarization [17,27]. Furthermore, the levels of proteins expression in the NF-κB signaling pathway were evaluated to explore the potential mechanism by which the ECH-Exos hydrogel modulated macrophages (Fig. 4H and I). The relative level of phosphorylated IκBα (p-IκBα) was significantly inhibited in the ECH-Exos group compared to the other groups (Fig. 4H and I). As an activator of the inflammatory NF-κB pathway, the p-IκBα can regulate the positive expression of pro-inflammatory cytokines [27,45]. Similarly, the expression of p-P65, the downstream factor of NF-κB, was significantly suppressed in the ECH-Exos group (Fig. 4H and I). Additionally, as displayed in Fig. 4H and I, the level of IκBα in the ECH was the lowest, whereas the levels of P65 proteins were comparable among groups. Overall, these findings suggested that the ECH-Exos hydrogel could regulate the polarization of macrophages from the M1 to M2 phenotype through downregulating the NF-κB signaling pathway.

Besides its potential to induce locomotive deficits, PNI yields pain mediated by inflammation [19–21]. Moreover, preexisting neuroinflammation in diabetics is likely to aggravate the inflammatory pain after PNI [19,22]. Furthermore, it has been found that electroconductive hydrogels slightly exacerbated the inflammation response by increasing the infiltration of M1 macrophages, which could not attenuate or evern possibly aggravate early pain after acute PNI [17]. It is generally agreed that interactions between the nervous and immune systems, termed "neuroimmune reactivity", trigger neuroinflammation causing aberrant sensory processing and subsequent pain [20,21,24,25]. In this respect, after nerve injury, NF-κB is activated, which further produces pro-inflammatory cytokines and chemokines to recruit macrophages/microglia into the lesion site to induce neuroinflammation and cause peripheral sensitization [20,21,25]. Subsequently, spontaneous activity from primary afferents elicited by neuroinflammation drives central sensitization. It is well-established that both peripheral and central sensitization contributes to persistent pain [20,21,25]. Indeed, macrophages/microglia play a major role in regulating neuroinflammation, and inflammatory pain after diabetic PNI has been extensively acknowledged [12,19–22,25]. Importantly, the inflammatory microenvironment around the damaged nerve induces pain and limits neural and axonal regeneration capacity [12,17,46]. Therefore, suppressing early-stage inflammation and modulating the M1/M2 macrophage polarization is vital for pain relief and nerve repair during diabetic PNI [10,12,17,19,22]. It has been reported that BMSCs have an excellent immunomodulatory capacity in regulating inflammatory pain and repairing injured tissues [17,24–26]. As primary paracrine soluble factors, BMSCs-derived Exos play an important role in the native immune system via intercellular communication [17,26]. With sizes

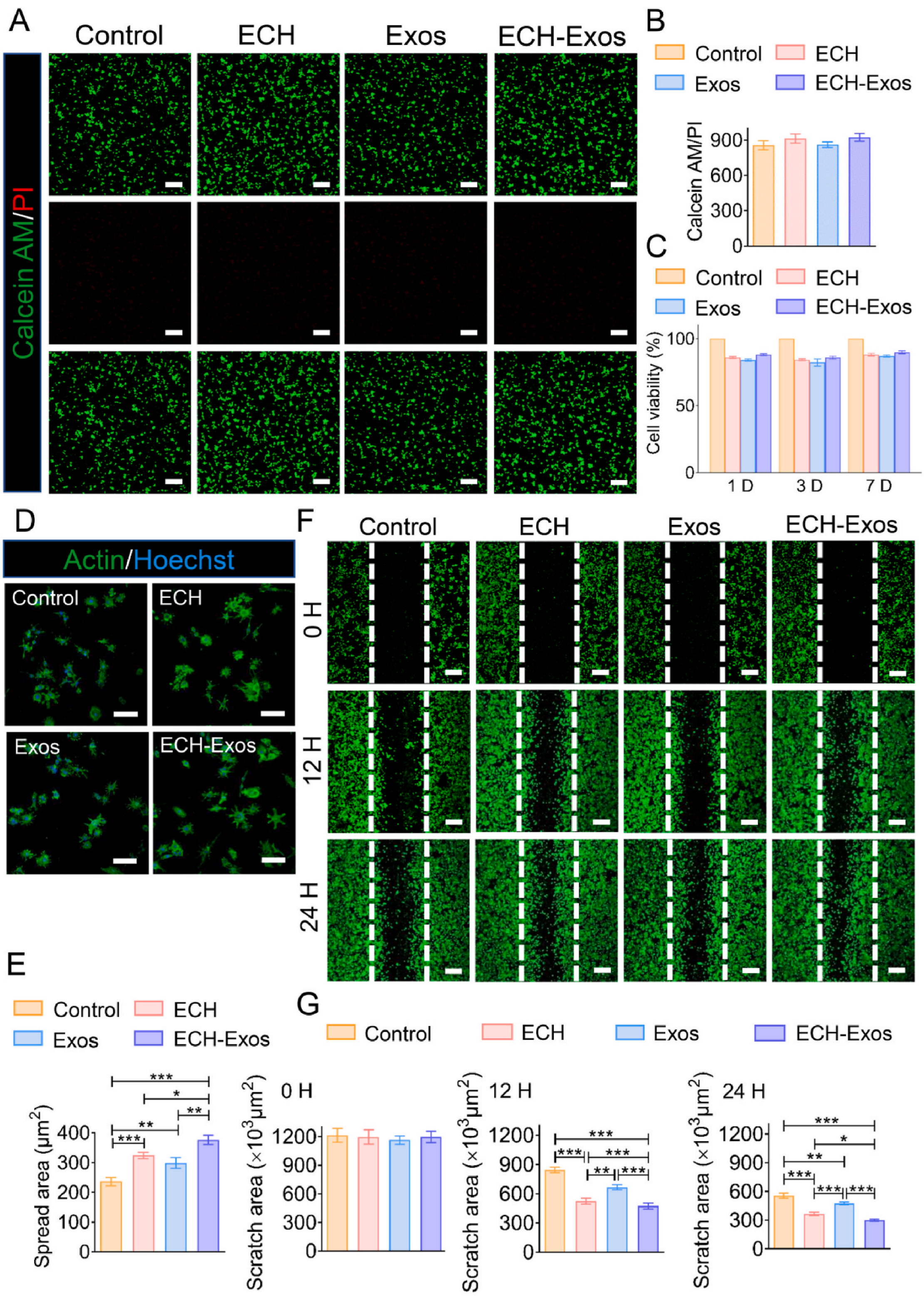

Fig. 3. In vitro SCs viability, adhesion and migration on the ECH-Exos. (A) Live/dead assay of the SCs cultured on each sample surface for 1 day. Live cells were stained in green and dead cells in red. The scale bar represents 200 μm. (B) Quantitative analysis of live/dead assay (n = 3). (C) The CCK-8 assay showed that all the cell viability surpassed 80% for each sample after seeding for 1, 3 and 7 days (n = 5). (D) The cytoskeleton images showed the adhesion of SCs cultured in each group after 3 days. The scale bar represents 50 μm. (E) Quantitative analysis of cell spread area (n = 9). (F) Wound-healing migration assay of the SCs on each sample at different time points. The scale bar represents 200 μm. (G) Quantitative analysis of the scratch area at the bare region at 0, 12, and 24 h (n = 3). Statistical differences were determined by using One-way ANOVA with Bonferroni's multiple comparison test (**P* < 0.05, ***P* < 0.01, and ****P* < 0.001).

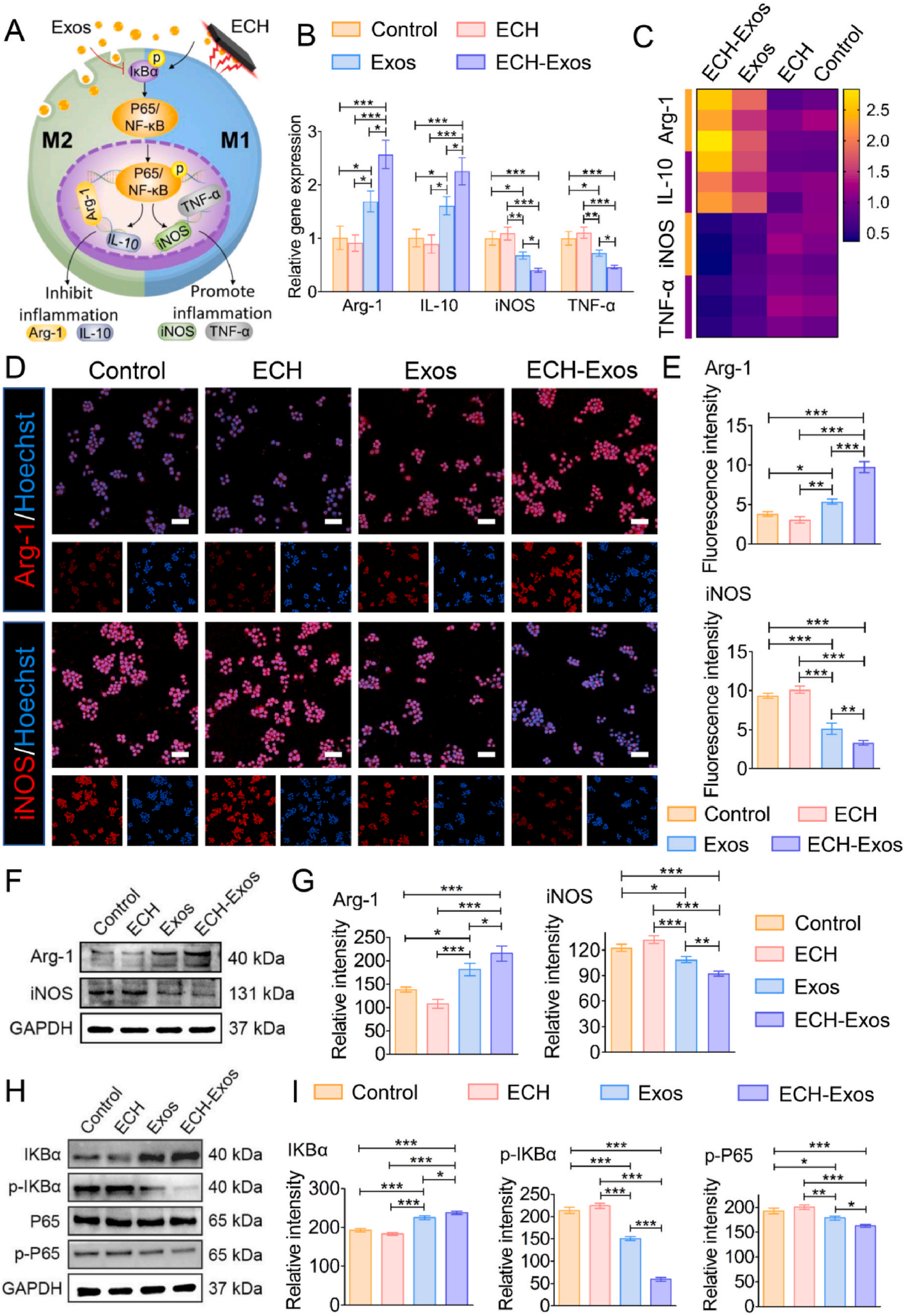

(caption on next page)

Fig. 4. ECH-Exos stimulated the polarization of RAW264.7 cells from M1 to M2 phenotype through the NF-κB pathway. (A) An illustration of ECH-Exos modulating the macrophage polarization from an M1 to M2 phenotype. (B) Column graph showing the RT-qPCR results on the gene expressions of anti-inflammatory cytokines (Arg-1 and IL-10) and pro-inflammatory cytokines (iNOS and TNF-α) in each group (n = 3). (C) Heat map showing the RT-qPCR results on the gene expressions of anti-inflammatory cytokines (Arg-1 and IL-10) and pro-inflammatory cytokines (iNOS and TNF-α) in each group (n = 3). (D) IF images displaying the amount of Arg-1 (red) positive and iNOS (red) positive RAW264.7 cells cultured on each group. The scale bar represents 50 μm. (E) Quantitative analysis of the fluorescence intensity of Arg-1 and iNOS (n = 3). (F) WB analysis of the Arg-1 and iNOS protein expression. (G) The protein band intensity of Arg-1 and iNOS was quantified using ImageJ (n = 3). (H) WB analysis of the expression of the related proteins of the NF-κB pathway. (I) Quantification of proteins related to the NF-κB pathway (n = 3). Statistical differences were determined by using One-way ANOVA with Bonferroni's multiple comparison test ($*P < 0.05$, $**P < 0.01$, and $***P < 0.001$).

ranging from 30 nm to 200 nm, Exos contain protein, lipid and miRNAs, specifically miR-199a, which induce the downregulation of genes related to the NF-κB pathway [17,27,28,47]. In our in vitro experiments, we combined an ECH with BMSCs-Exos for attenuating inflammatory response and enhancing axonal regeneration. After validating mechanical, electroconductive, and self-curling properties and sustained Exos release, PC-12 cells and SCs co-cultured with the ECH-Exos system exhibited potent viability and activity attributed to the synergistic stimulatory effect of the ECH hydrogel and Exos. Furthermore, after RAW264.7 cells were cultured on the ECH-Exos, we found an upregulation of anti-inflammatory cytokines and significant downregulation of pro-inflammatory cytokines by promoting the polarization of macrophages from the M1 to M2 phenotype mediated by the NF-κB signaling pathway. Thus, we conclude that the ECH-Exos hydrogel has favorable mechanical, electroconductive, self-curling, and Exos-releasing properties. Moreover, we demonstrated its in vitro biocompatibility, axonal regeneration-related markers expression, and in vitro inflammatory capacity, suggesting it is suitable for implantation around damaged nerves in rats with DM. Our findings substantiate that the ECH-Exos hydrogel has an in vitro dual therapeutic effect, including supression of inflammation and nerve regeneration.

3.6. In vivo biocompatibility evaluation of ECH-Exos hydrogel

Before transplantation of electroconductive hydrogel into animals, in vivo biocompatibility, including hemocompatibility (hemolytic ratio and levels of serum protein) and histological analysis of five major organs (heart, liver, spleen, lung, and kidney), was assessed. It is well-established that hemocompatibility is a vital index used to analyze the in vivo hemolytic properties of foreign materials [5,17]. Fig. S5A clearly showed that serum isolated from materials (ECH, Exos, and ECH-Exos) co-incubated whole blood presented light yellow color, similar to the control group (PBS), whereas the Triton-100X group exhibited a bright red color. The OD value of serum obtained from the three different materials was comparable to the control group (PBS) and significantly lower compared to the Triton-100X group (Fig. S5B). The percentage of hemolysis of the three materials groups was below 1.1%, indicating that the ECH-Exos possessed excellent hemocompatibility. Furthermore, the histological analysis validated that there was no deposition of hydrogel degradation products and no apparent pathological abnormalities in the five major organs in the rats implanted with hydrogels (Fig. S5C). Additionally, the differences in the levels of serum protein were not statistically significant, including ALT, AST, and TP among the PNI, ECH, Exos, and ECH-Exos groups, suggesting the hydrogels yielded no systemic toxicity (Fig. S5D). Overall, our ECH-Exos hydrogel is safe and suitable for treating diabetic PNI, given its favorable in vitro and in vivo biocompatibility [5,16,17,36].

3.7. The ECH-Exos hydrogel relieved inflammatory pain in diabetic rats after PNI

It is well-established that the degree of mechanical allodynia and thermal hyperalgesia can be quantified by PWT (via von-Frey filaments) and TWL (by hot plate), respectively [37,38,40]. Indeed, increased PWT or TWL indicates a decrease in mechanical allodynia or thermal hyperalgesia. Therefore, to validate whether ECH-Exos hydrogel could yield pain relief in diabetic rats after PNI, PWT and TWL were applied to assess the sensitivity of mechanical pain and thermal hyperalgesia (Fig. 5A, D). As presented in Fig. 5B and C, after sciatic nerve injury, rats treated with ECH or without exogenous implantation exhibited a significant decrease in PWT from baseline, while rats treated with ECH-Exos hydrogel showed a significant increase in PWT from baseline. Although the PWT in the Exos group also increased from baseline and was greater than that in ECH and PNI groups at the beginning, their disparities almost disappeared from postoperative day 5 (Fig. 5B). This finding suggested that the monotherapy with Exos could relieve pain after PNI, but the in vivo rapid and burst release of Exos limited their long-acting pain relief. Importantly, after the Exos were loaded in ECH via reversible noncovalent hydrogen bonds, the PWT was significantly greater compared to the other three groups after the 2-week experimental period, which illustrated that the ECH could ensure the sustained release of Exos and yielded corresponding pain relief for up to 14 days (Fig. 5B and C). Consistently, the TWL in the ECH-Exos group was significantly longer than the other groups, implying these animals experienced hypoalgesia (suffered less pain) (Fig. 5E and F). Interestingly, the PWT and TWL in the ECH group were slightly lower than in the PNI group. Although there was no significant difference, implantation of ECH alone could not attenuate or worsen pain during acute PNI (Fig. 5B, C, E, F). To validate that the ECH-Exos hydrogel relieved pain via suppressing the inflammatory reaction around the injured nerve, IF and WB assays were used to evaluate the expression of iNOS 4 weeks after PNI (Fig. 5G, H, I, J). The density of iNOS-positive cells was slightly higher at the lesion site in the ECH group than in the PNI group, suggesting that the ECH exacerbated local inflammation to some extent (Fig. 5G and H). Implantation of the ECH-Exos caused a significant reduction of the density of iNOS-positive cells, which was approximately 31%, 33%, and 45% of that in the PNI group, ECH group, and Exos group, respectively (Fig. 5G and H). In accordance with the IF results, the expression level of iNOS protein was the highest in the ECH group and lowest in the ECH-Exos group (Fig. 5I and J). Taken together, these results illustrated that the ECH-Exos hydrogel could attenuate pain by inhibiting the inflammatory response at the injury site.

Although electroconductive hydrogels have been reported to effectively repair damaged nerves, their application in pain relief following PNI has been largely understudied [5,15–17]. Hence, we aimed to design an electroconductive hydrogel with the capacity to attenuate inflammatory pain to ensure satisfactory repair after PNI. Consistent with the literature, our electroconductive hydrogel acted as a foreign body and induced a mild inflammatory reaction, potentially exacerbating pain after PNI [17]. Nonetheless, this limitation was overcome after the embedment of BMSCs-Exos with anti-inflammatory ability. In this respect, the sustained release of BMSCs-Exos from ECH-Exos system provided better long-acting analgesia than Exos alone. Therefore, the present study substantiated that the ECH-Exos hydrogel could relieve inflammatory pain after diabetic PNI.

3.8. Morphological and functional assessment of regenerated nerves

Besides its ability to attenuate pain, this study examined whether the ECH-Exos hydrogel could promote nerve repair (Fig. 6A). As seen in Fig. 6B, the laminar hydrogel dressing was easily affixed to an injured nerve (length 5 mm), automatically forming a tube-like structure. The morphological structure of the sciatic nerve after injury is tightly associated with locomotor function recovery. Consequently, histological

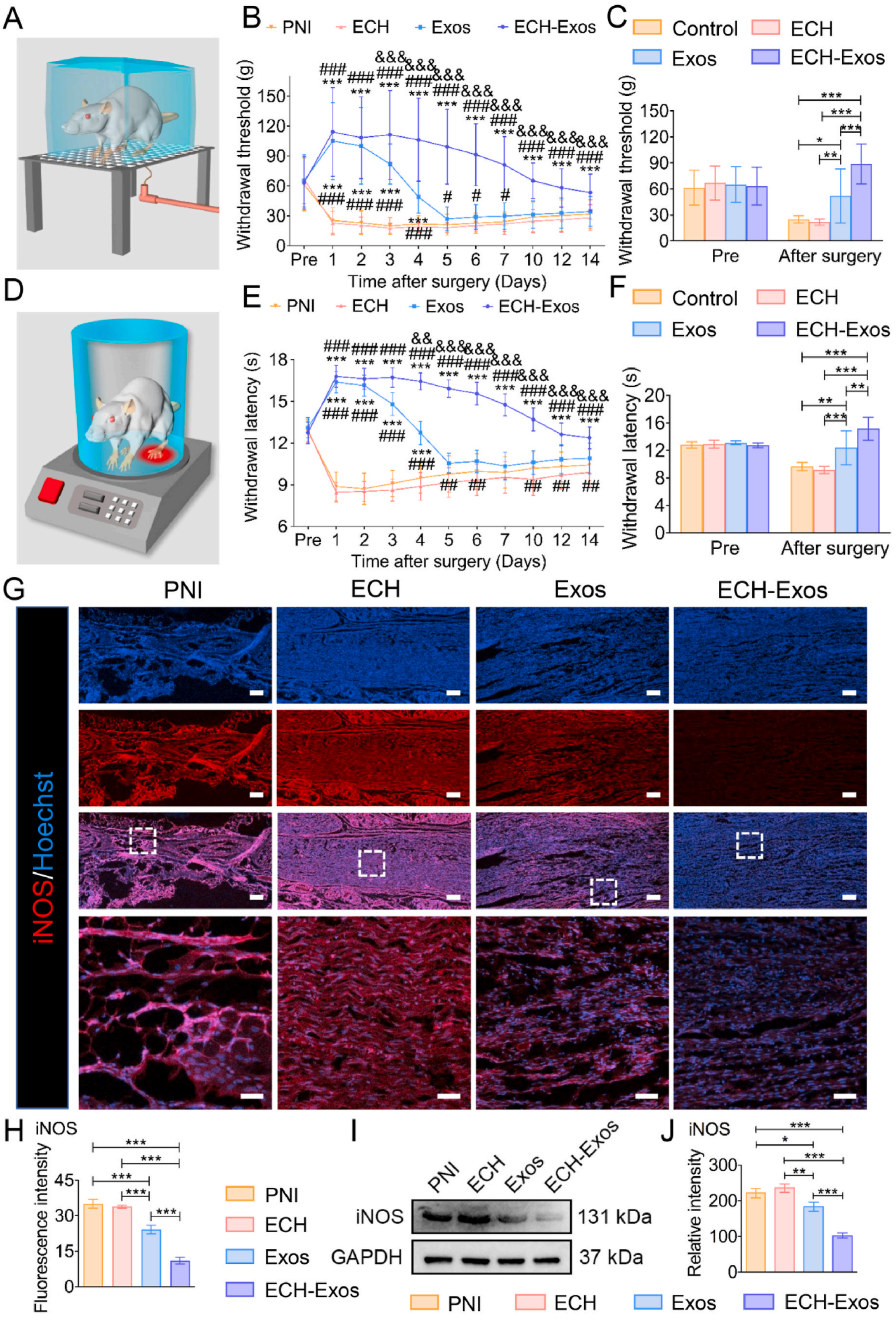

(caption on next page)

Fig. 5. The ECH-Exos relieved inflammatory pain in diabetic rats after PNI. (A) Illustration of mechanical allodynia assay with von-Frey filaments. (B) Changes in PWT in each group after diabetic PNI compared to baseline (before model establishment) (n = 8). (C) Average PWT shown by different study groups before and after surgery (n = 8). (D) Illustration of thermal hyperalgesia response by hot plate assay. (E) Changes in TWL in each group after diabetic PNI compared to baseline (before model establishment) (n = 8). (F) Average TWL shown by different study groups before and after surgery (n = 8). (G) IF images showed that the iNOS-positive cells (red) were significantly decreased in the ECH-Exos group compared with other treatments and PNI conditions. The scale bar represents 200 μm at low magnification and 50 μm at high magnification. (H) The intensity of iNOS fluorescence signals was quantitatively analyzed (n = 3). (I) WB analysis of the in vivo iNOS protein expression. (J) The protein band intensity of iNOS was quantified by using ImageJ (n = 3). Statistical differences were determined by using the nonparametric Kruskal-Wallis test when analyzing the PWT and TWL or One-way ANOVA with Bonferroni's multiple comparison test when comparing IF and WB results (* = significantly different from the PNI group, # = significantly different from the ECH group, & = significantly different from the Exos group; *, #, & $P <$ 0.05, **, ##, && $P <$ 0.01, and ***, ###, &&& $P <$ 0.001).

analyses, including HE and MTS, were performed, and the results revealed that the regenerated axon fibers in the ECH-Exos group were highly enriched and well-arranged at the lesion site (Fig. 6C and D). Besides, the nerve fibers in the ECH and Exos groups exhibited moderate repair effects (Fig. 6C and D). Nevertheless, the axonal fibers in the PNI group without any treatment were sparse, slim, and disorganized, with a significantly damaged region (Fig. 6C and D). Consequently, this ECH-Exos dressing provided a supporting extracellular microenvironment for axon regrowth. SFI is a widely used indicator to analyze the recovery of locomotor function after PNI. This index is calculated according to several footprint parameters, which include PL, TS, and ITS, ranging from −100 (complete dysfunction) to 0 (normal function) (Fig. 6E) [5]. The lack of nerve and muscle function after PNI can cause changes in footprint measurements, such as an increment in the PL but a reduction in the TS and ITS [5]. As shown in Fig. 6F, after four weeks of PNI, treatment with both electroconductive hydrogels, especially the ECH-Exos group, yielded clear footprints with superior TS and ITS, whereas both the PNI and Exos groups exhibited inferior TS and ITS and impaired ankle movement. After two weeks, motor function recovery was stabilized until the end of our experiment. Consistently, motor function in rats treated with the ECH-Exos (score = −42.72 ± 1.95) improved significantly compared to the PNI group (score = −75.99 ± 1.95), ECH group (score = −50.71 ± 2.34) and Exos group (score = −71.59 ± 1.81) four weeks after surgery (Fig. 6G). Additionally, the SFI score in the ECH group was significantly greater compared to the PNI and Exos groups as from two weeks postoperatively (Fig. 6G). Overall, although the capacity of regenerating nerve fibers in the Exos group was inferior to the ECH group, the combination of Exos with ECH yielded a synergistic effect to enhance the regeneration of axonal fibers at the lesion as well as the recovery of motor function after PNI.

3.9. In vivo axonal regeneration and remyelination

Since NF-200 protein is a primary indicator of neurofilament regeneration, longitudinal nerve sections were examined by IF staining to detect the effect of axonal regeneration after four weeks of treatment. The NF-positive axons exhibited a tight linear distribution at the lesion site in the ECH-Exos group (Fig. 7A). Furthermore, quantification of the axonal density at the damaged site showed that it was highest in the ECH-Exos treatment, relatively low in the ECH group, and significantly lower in the Exos and PNI groups (Fig. 7B). We next stained for the myelin basic protein (MBP) to evaluate the degree of remyelination of regenerated axons. As shown in Fig. 7A, MBP-positive cells were well-oriented and exhibited an orderly arrangement in nerves treated with ECH-Exos. In contrast, MBP-positive cells were sparse and exhibited a disordered arrangement in nerves not treated with electroconductive hydrogels, especially in the PNI group. Moreover, the density of MBP-positive fibers was comparable to NF-positive fibers among groups (Fig. 7B). In accordance with the IF analyses, WB results validated that the expressions of NF and MBP protein in the ECH-Exos group were significantly upregulated compared to the other groups at the injury site (Fig. 7C and D). The above results substantiate that the ECH-Exos treatment can facilitate myelinated nerve regeneration after PNI.

Additionally, S-100β is another indicator of remyelination and a specific marker of SCs migration. In our study, the S-100β positive fibers showed a highly regular and linear arrangement around the lesion site in the ECH-Exos group (Fig. 8A). Besides, S-100β positive staining in the ECH-Exos group was 2.1-fold, 1.4-fold, and 1.8-fold higher than in the PNI, ECH, and Exos groups, respectively, suggesting that the SCs contributed to the formation of myelin sheaths (Fig. 8B). Furthermore, WB analysis confirmed that the protein expression of the S-100β in the ECH-Exos group was significantly higher than the other groups (Fig. 8C and D). These findings further validated that the ECH-Exos dressing significantly enhanced the remyelination of the regenerated axon. Interestingly, the effect of myelinated nerve regeneration in the single ECH group was better compared to treatment with Exos only, which may be due to the rapid in vivo release of Exos, although they have been reported to significantly promote axonal growth [17,48]. Meanwhile, the ECH scaffold continuously provides a beneficial microenvironment to support the regrowth of myelin-associated axonal regeneration [5,16]. Current evidence suggests that innate bioelectrical activity plays a crucial role in neural maturation and function. Cell-to-cell communications between the neurons and precursors via spontaneous electrical signals are essential for regeneration events, such as neuron differentiation, development, migration, remyelination, and the formation of neurotransmitter phenotypes [5,16]. As an electroconductive bridge, the ECH allows stable electrical interactions between electrogenic neural tissues, facilitating axonal regrowth and remyelination [5,15,16].

There is a growing consensus that the MEK/ERK signal pathway is essential for modulating neuronal activity and axonal outgrowth [5,15,49]. Electrical signaling is correlated to the activation of these pathways [5]. To examine the potential mechanisms of ECH-Exos facilitating axon regeneration and remyelination, the protein expressions of the MEK/ERK pathway were investigated by WB. The relative expression levels of p-MEK and p-ERK were significantly upregulated in the ECH-Exos group (Fig. 8E and F). Nevertheless, the expression of the corresponding unphosphorylated proteins was comparable among the four groups (Fig. 8E). These results substantiate that the ECH-Exos hydrogel enhanced axonal myelination and extension by activating the MEK/ERK pathway.

3.10. TBS and TEM assessment

Tissue cross-sections were prepared for TBS and TEM analyses to evaluate the remyelination of the regrown sciatic nerve. TBS results showed that the myelination of the regenerated nerve in the ECH-Exos-treated models was better than in the other groups. In this respect, the myelin sheath in the PNI group was sparse and messy (Fig. 9A). The TEM images showed that the regenerated axons in the ECH-Exos group were surrounded by thick and electron-dense myelin sheath structure, whereas those in the PNI and Exos groups were accompanied with thin and electron-sparse myelinated structure (Fig. 9B). Notably, vacuole-like defects could be observed in the myelin sheaths among all groups, probably secondary to demyelination induced by DM (Fig. 9B). Furthermore, the specific morphological parameters of the nerve fibers, including the diameter and area of the myelinated axon, myelin sheath thickness, and G-Ratio, were quantified and compared during TEM analysis [5]. It was found that both the myelinated axon diameters and myelinated axon area in the ECH-Exos group were larger than in the other groups (Fig. 9C and D). Besides, the myelin sheath thickness was

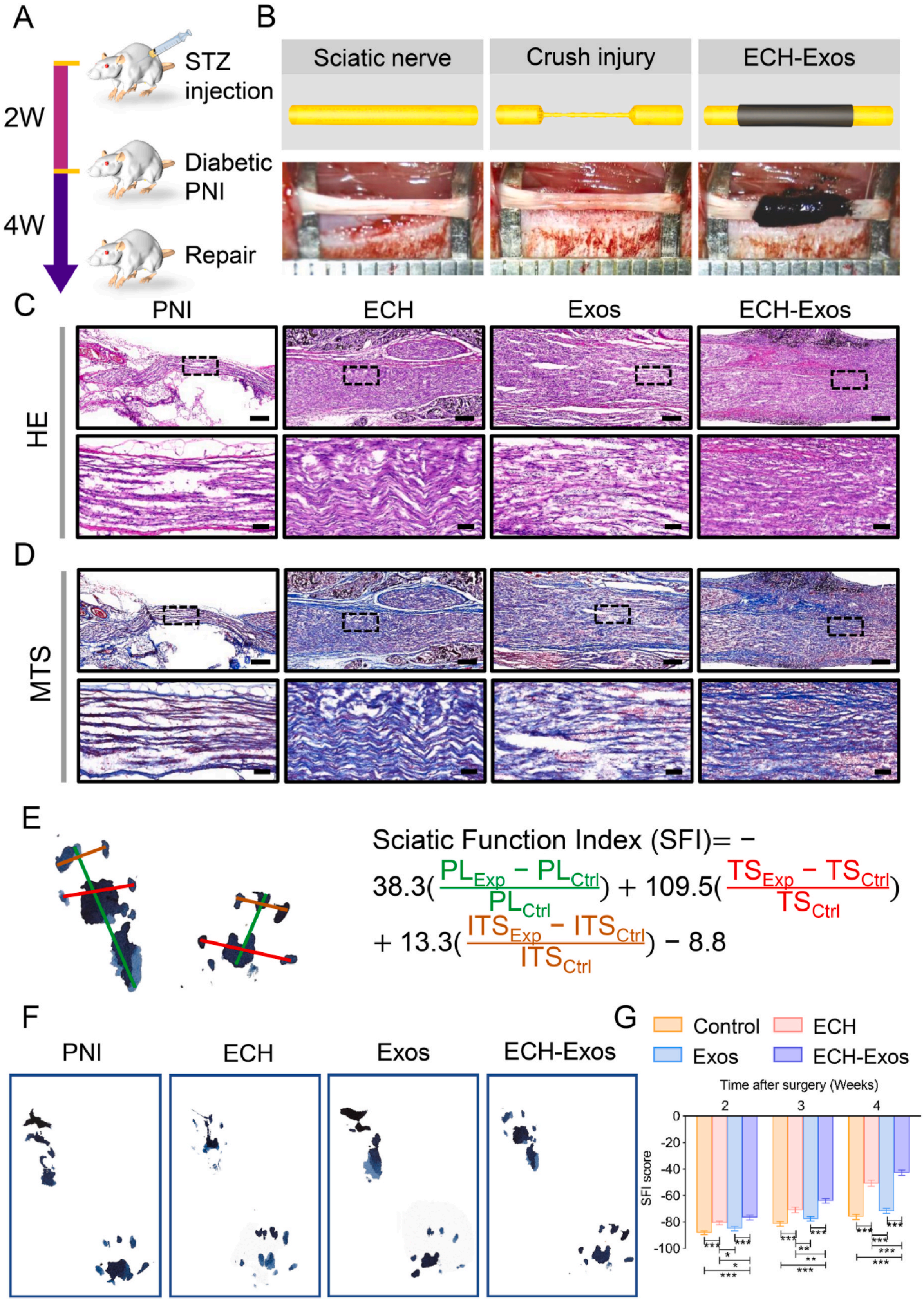

Fig. 6. Morphological and functional assessment of regenerated nerves. (A) Illustration showing the repair process of diabetic PNI. (B) Illustrations and photographs showing the implantation of ECH-Exos dressing around the crushed sciatic nerve in a diabetic rat. (C–D) HE staining and MTS presented the structural repair of the sciatic nerve after 4 weeks of treatment. The scale bar represents 500 μm at low magnification and 100 μm at high magnification. (E) The formula for calculating the SFI consisted of different footprint parameters. (F) Representative photographs of the footprints. (G) SFI scores of different study groups 2, 3, and 4 weeks after the procedure (n = 4). Statistical differences were determined by using One-way ANOVA with Bonferroni's multiple comparison test ($*P < 0.05$, $**P < 0.01$, and $***P < 0.001$).

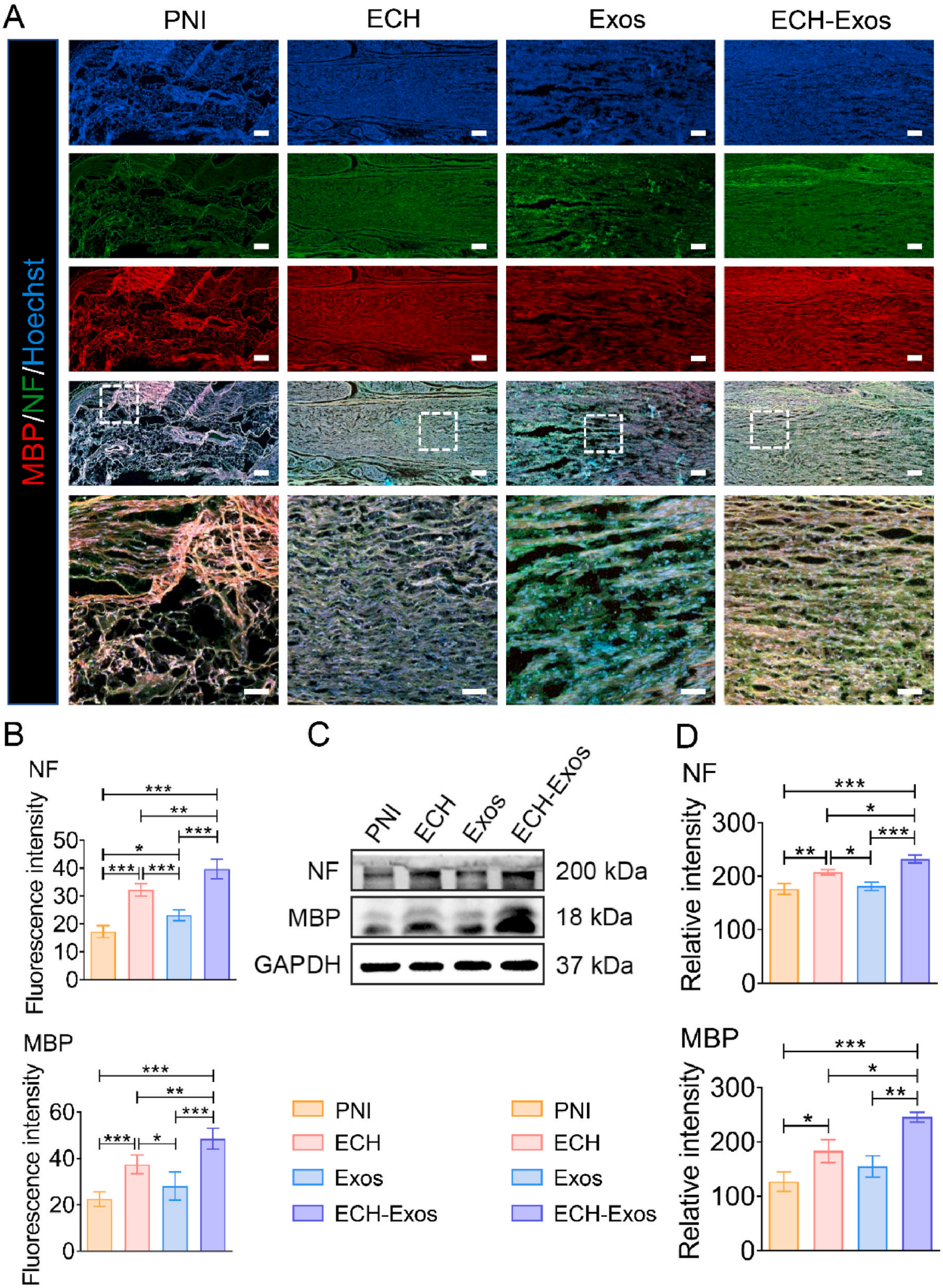

Fig. 7. Enhancement of axon regrowth with ECH-Exos treatment in diabetic PNI models. (A) IF staining of the NF (green) and MBP (red) proteins in the injured sciatic nerve tissues after 4 weeks of treatment. The scale bar represents 200 μm at low magnification and 50 μm at high magnification. (B) Quantification of the fluorescence intensity of NF and MBP proteins (n = 3). (C) WB analysis of the proteins expression of in vivo NF and MBP. (D) Quantitative measurement of protein band intensity of NF and MBP (n = 3). Statistical differences were determined by using One-way ANOVA with Bonferroni's multiple comparison test (**P* < 0.05, ***P* < 0.01, and ****P* < 0.001).

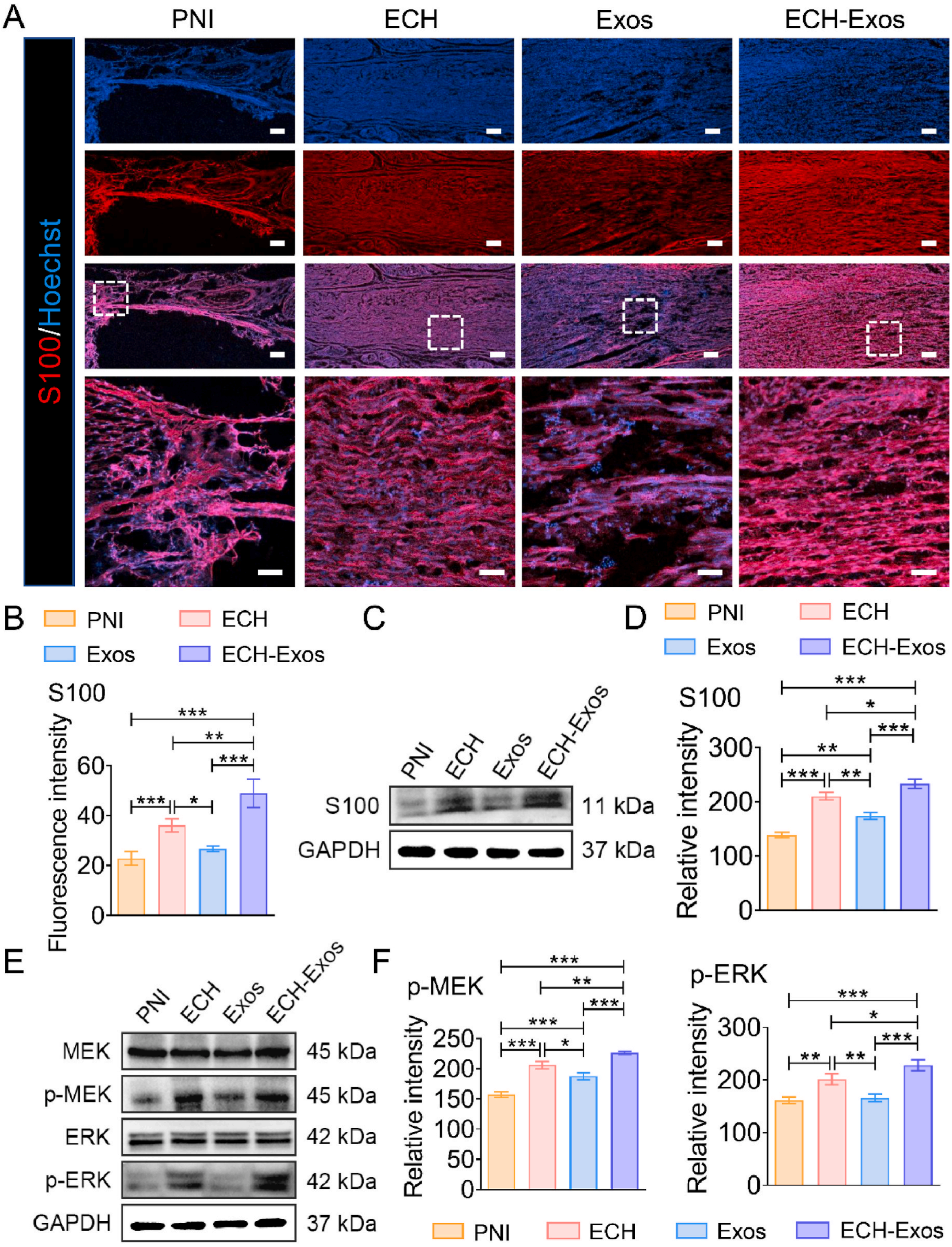

Fig. 8. ECH-Exos treatment promoted remyelination of the regenerated axons. (A) IF staining of the S100β (red) proteins in the injured sciatic nerve tissues after 4 weeks of treatment. The scale bar represents 200 μm at low magnification and 50 μm at high magnification. (B) Quantification of the fluorescence intensity of S100β proteins (n = 3). (C) WB analysis of the proteins expression of in vivo S100β. (D) Quantitative measurement of protein band intensity of S100β (n = 3). (E) WB analysis of the relative expression of the MEK/ERK pathway proteins. (F) The protein band intensity of the MEK/ERK pathway proteins was quantified (n = 3). Statistical differences were determined by using One-way ANOVA with Bonferroni's multiple comparison test (*$P < 0.05$, **$P < 0.01$, and ***$P < 0.001$).

the highest while the G-Ratio was the lowest following treatment with ECH-Exos (Fig. 9E and F). The G-Ratio refers to the ratio of the internal axon diameter to the total external nerve fiber diameter and is reportedly associated with the rate of electric conduction, considered as an indicator of axon function and integrity. It is widely acknowledged that a smaller G-ratio reflects better remyelination of the regenerated nerves. A previous study found that the G-ratio of the sciatic nerve in young rats without injury and DM was lower than the ECH-Exos group in this study

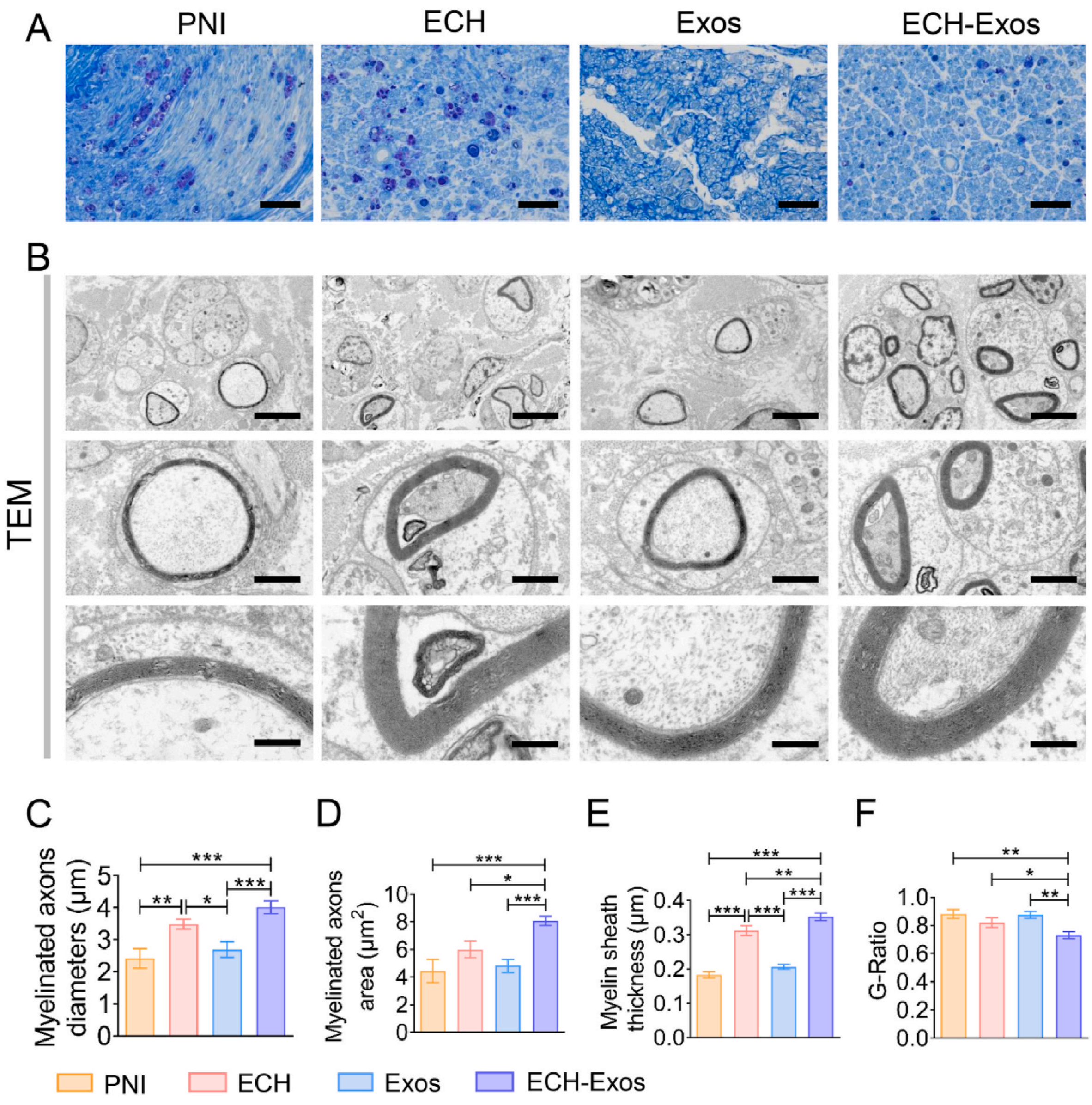

Fig. 9. Morphological assessment of the axonal remyelination using TBS and TEM. (A) TBS displaying the remyelination of the regenerated axon. The scale bar represents 50 μm. (B) Representative TEM images of the myelinated axonal regrowth. Scale bar respectively represents 5 μm at low magnification, 2 μm at median magnification and 500 nm at high magnification. (C–F) Quantitative analysis of the myelination of the regenerated axons with four parameters, including (C) myelinated axon diameter, (D) myelinated axon area, (E) myelin sheath thickness, and (F) G-Ratio (n = 3). Statistical differences were determined by using One-way ANOVA with Bonferroni's multiple comparison test (*$P < 0.05$, **$P < 0.01$, and ***$P < 0.001$).

(0.60 ± 0.04 vs. 0.73 ± 0.02) [50], which may be due to the fact that our G-ratio was acquired from diabetic and damaged sciatic nerves following treatment with ECH-Exos. Nonetheless, the above results substantiated that the demyelinated and injured nerves in diabetic rats could be effectively repaired by ECH-Exos implantation.

3.11. Alleviation of gastrocnemius muscle atrophy

Given that the attenuation of gastrocnemius muscle atrophy can represent motor function recovery after sciatic nerve injury, gross views and histological examinations were obtained four weeks after surgery. As exhibited in Fig. 10A, the gastrocnemius muscle obtained from the injured side was significantly atrophied compared to the contralateral side, specifically in the PNI and Exos groups. Histological examinations, including HE and MTS, were conducted to observe structural changes in the gastrocnemius muscle (Fig. 10B and C). Significant atrophy was found in the PNI and Exos groups with slim and disorderly muscle fibers, in addition to large amounts of hyperplastic collagen fibers deposited. Importantly, these findings were significantly improved after treatment with the electroconductive hydrogels, especially with the implantation of ECH-Exos, which yielded well arranged and stouter muscle fibers and fewer collagen deposits (Fig. 10B and C). Greater gastrocnemius muscle weight and larger fiber area further indicated that the application of the ECH-Exos effectively promoted the restoration of atrophied muscle fibers (Fig. 10D and E). Moreover, the area of collagen fiber deposits in the ECH-Exos group exhibited a three-fold, two-fold, and three-fold decrease compared to the PNI and Exos groups (Fig. 10F). Taken together, the above findings substantiated that the ECH-Exos hydrogel could restore muscle morphology and function as well as attenuate muscle atrophy.

Overall, our in vivo experiments found that treatment with ECH alone yielded better performance in repairing nerve damage and restoration of locomotor function in rats with DM compared with pure Exos treatment. Furthermore, the application of Exos alone still yielded mild

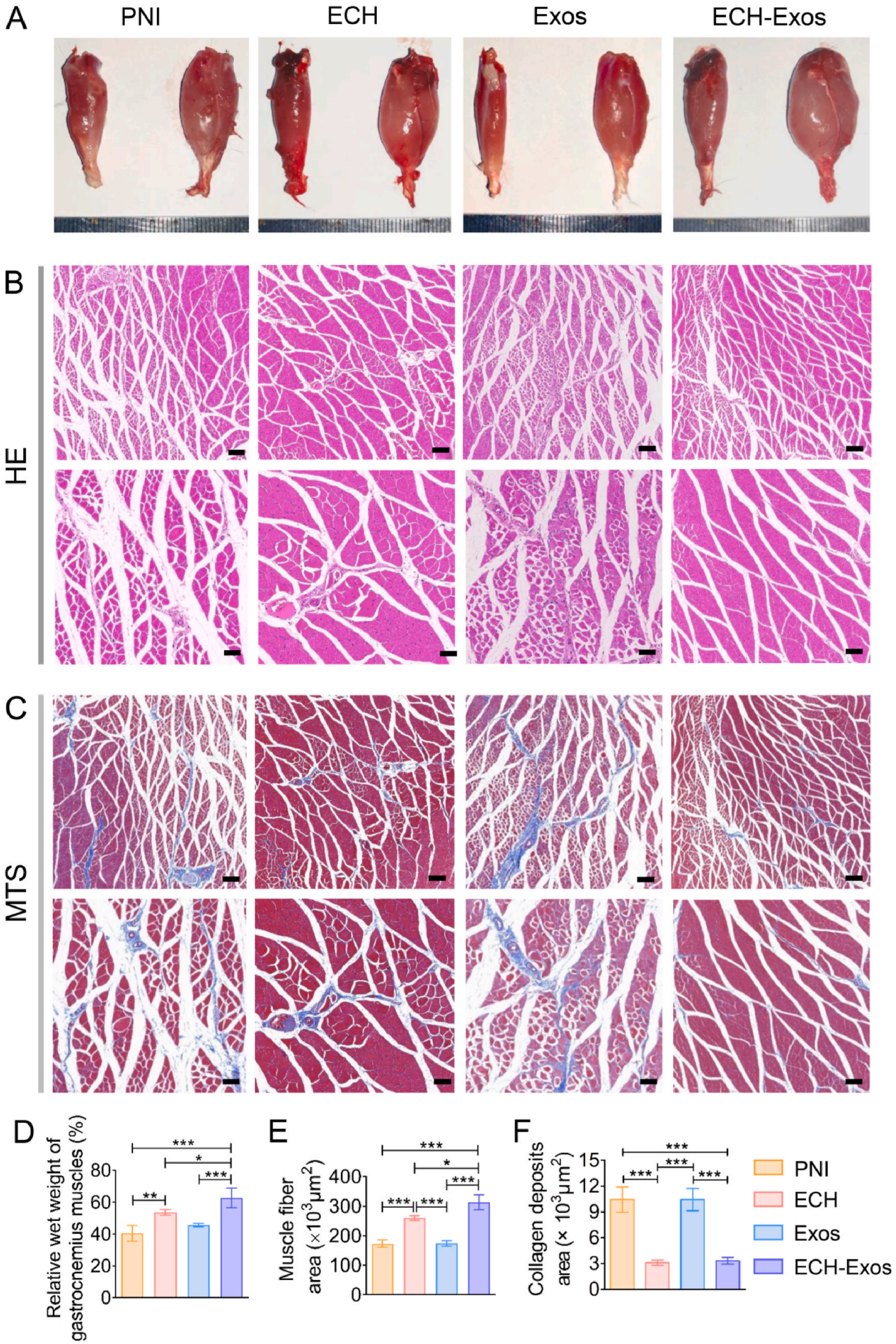

Fig. 10. ECH-Exos treatment ameliorated gastrocnemius muscle atrophy. (A) Gross photographs of the separated gastrocnemius muscles in each group. (B) HE staining shows the cross-sectional images of the ipsilateral muscles. The scale bar represents 200 μm at low magnification and 50 μm at high magnification. (C) MTS presenting the collagen deposits on the cross-sectional images of the ipsilateral muscles. The scale bar represents 200 μm at low magnification and 50 μm at high magnification. (D) Quantitative analysis of the relative wet weight of the gastrocnemius muscle (n = 3). (E) Quantitative analysis of the area of muscle fiber (n = 3). (F) Quantitative analysis of the area of collagen deposits (n = 3). Statistical differences were determined by using One-way ANOVA with Bonferroni's multiple comparison test (*$P < 0.05$, **$P < 0.01$, and ***$P < 0.001$).

repair ability compared with the PNI group though the difference between these two groups was not statistically significant. Interestingly, it has been established that both ECH and Exos can facilitate axonal regeneration [5,15–17,48]. Nonetheless, in vivo treatment with Exos alone could not ensure the sustained release and quick diffusion around the lesion and could not meet the requirements of PNI repair. Regarding ECH, our previous works and the present study found that this electroconductive hydrogel was relatively stable and capable of maintaining the repairing efficiency at least four weeks after PNI [5,16]. However, ECH as exogenous materials implanted into the body could induce a mild inflammatory response, which was not beneficial for nerve regrowth and even aggravated the inflammatory pain after PNI with DM [17]. Interestingly, after the combination of ECH and the anti-inflammatory BMSCs-Exos via reversible hydrogen bonding, the repairing capacity was greatly improved due to the sustained release of Exos and synergistic enhancement of neural regeneration through the MEK/ERK pathway (Fig. 11). Additionally, the ECH-Exos system could alleviate early inflammatory pain via the NF-κB pathway, thereby achieving a satisfactory dual repair effect on diabetic PNI, including restoration of motor function and pain relief (Fig. 11).

4. Conclusion

In summary, a soft, tissue-adhesive, electroconductive, and biocompatible ECH combined with BMSCs-Exos was developed in this study, which demonstrated an outstanding ability to promote myelin-associated axonal regeneration and attenuate inflammatory pain for diabetic PNI. ECH was prepared by the mixture of TA, Py, and Fe^{3+}, similar to a wound or surgical dressing. The Exos were immobilized on the ECH via the formation of reversible noncovalent hydrogen bonds, allowing their sustained release and accumulation around the lesion site, thereby meeting the demands of alleviating inflammatory pain during early PNI. Importantly, the laminar hydrogel dressing could easily adhere to the nerve tissues and automatically wrapped a size-matched tube-like structure, simplifying the inconvenient implantation process during the treatment of diabetic PNI. The ability of the ECH-Exos system to promote SCs attachment and migration was demonstrated by our in vitro experiments. With the capacity to modulate macrophage polarization from M1 to M2 phenotype through the NF-κB pathway, the immunomodulatory Exos in this system compensated for the limitations of treatment with ECH alone. Furthermore, our in vitro and in vivo experiments validated that ECH-Exos could enhance myelinated axonal regrowth via the MEK/ERK pathway, thereby

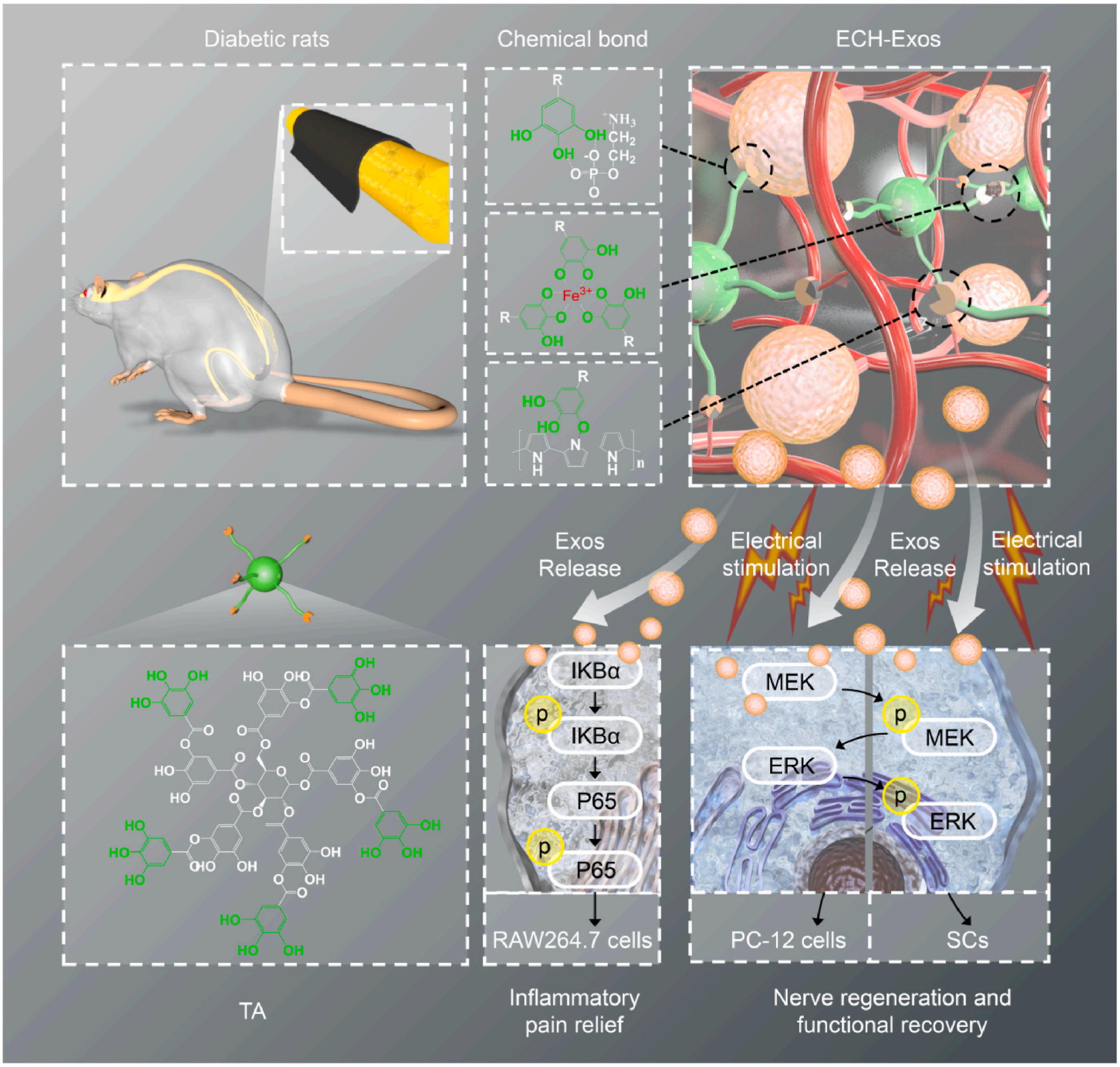

Fig. 11. The functional groups, chemical bonds and putative mechanism of ECH-Exos in attenuating inflammatory pain and promoting nerve regeneration and functional restoration after diabetic PNI.

improving muscle denervation atrophy and facilitating functional restoration in diabetic rats. This ECH-Exos composite provides a promising therapeutic strategy for promoting nerve regeneration and locomotor function restoration and relieving inflammatory pain after diabetic PNI.

Funding

This work was supported by the President Foundation of Nanfang Hospital, Southern Medical University (2020C024) and the Natural Science Foundation of Fujian Province (2021J011156).

Ethics approval and consent to participate

All animal experiments were performed after the approvement of the Animal Experimental Ethics Committee of Nanfang Hospital of Southern Medical University and complied with the requirements of the National Institutes of Health Guide for the Care and Use of Laboratory Animals.

CRediT authorship contribution statement

Qinfeng Yang: Conceptualization, Methodology, Formal analysis, Validation, Investigation, Writing – original draft. **Shenghui Su:** Methodology, Formal analysis, Validation, Funding acquisition. **Shencai Liu:** Methodology, Validation, Formal analysis. **Sheng Yang:** Methodology, Validation, Formal analysis. **Jing Xu:** Visualization, Investigation. **Yixiu Zhong:** Formal analysis, Visualization. **Yusheng Yang:** Formal analysis, Validation. **Liangjie Tian:** Methodology, Validation. **Zilin Tan:** Formal analysis, Investigation. **Jian Wang:** Resources, Visualization. **Zhiqiang Yu:** Resources, Supervision, Data curation. **Zhanjun Shi:** Resources, Visualization. **Fangguo Liang:** Methodology, Funding acquisition, Supervision.

Declaration of competing interest

The authors declare that they have no known competing financial interests or personal relationships that could have appeared to influence the work reported in this paper.

Acknowledgments

We thank Lei Fan for his help in drawing the schematic diagram and typesetting figures.

Appendix A. Supplementary data

Supplementary data to this article can be found online at https://doi.org/10.1016/j.bioactmat.2023.02.024.

References

[1] T. Lin, S. Liu, S. Chen, S. Qiu, Z. Rao, J. Liu, S. Zhu, L. Yan, H. Mao, Q. Zhu, D. Quan, X. Liu, Hydrogel derived from porcine decellularized nerve tissue as a promising biomaterial for repairing peripheral nerve defects, Acta Biomater. 73 (2018) 326–338, https://doi.org/10.1016/j.actbio.2018.04.001.

[2] S. Vijayavenkataraman, Nerve guide conduits for peripheral nerve injury repair: a review on design, materials and fabrication methods, Acta Biomater. 106 (2020) 54–69, https://doi.org/10.1016/j.actbio.2020.02.003.

[3] R. Li, Y. Li, Y. Wu, Y. Zhao, H. Chen, Y. Yuan, K. Xu, H. Zhang, Y. Lu, J. Wang, X. Li, X. Jia, J. Xiao, Heparin-poloxamer thermosensitive hydrogel loaded with bFGF and NGF enhances peripheral nerve regeneration in diabetic rats, Biomaterials 168 (2018) 24–37, https://doi.org/10.1016/j.biomaterials.2018.03.044.

[4] Y. Cai, Q. Huang, P. Wang, K. Ye, Z. Zhao, H. Chen, Z. Liu, H. Liu, H. Wong, M. Tamtaji, K. Zhang, F. Xu, G. Jin, L. Zeng, J. Xie, Y. Du, Z. Hu, D. Sun, J. Qin, X. Lu, Z. Luo, Conductive hydrogel conduits with growth factor gradients for peripheral nerve repair in diabetics with non-suture tape, Adv. Healthc. Mater. 11 (2022) 1–12, https://doi.org/10.1002/adhm.202200755.

[5] C. Liu, L. Fan, Z. Tian, H. Wen, L. Zhou, L. Rong, B. Liu, Bioactive Materials Self-curling electroconductive nerve dressing for enhancing peripheral nerve regeneration in diabetic rats, Bioact. Mater. 6 (2021) 3892–3903, https://doi.org/10.1016/j.bioactmat.2021.03.034.

[6] K. Liu, L. Yan, R. Li, Z. Song, J. Ding, B. Liu, X. Chen, 3D printed personalized nerve guide conduits for precision repair of peripheral nerve defects, Adv. Sci. 9 (2022) 1–22, https://doi.org/10.1002/advs.202103875.

[7] H. Samadian, H. Maleki, A. Fathollahi, M. Salehi, S. Gholizadeh, H. Derakhshankhah, Z. Allahyari, M. Jaymand, Naturally occurring biological macromolecules-based hydrogels: potential biomaterials for peripheral nerve regeneration, Int. J. Biol. Macromol. 154 (2020) 795–817, https://doi.org/10.1016/j.ijbiomac.2020.03.155.

[8] A.S. Burahee, A.D. Sanders, C. Shirley, D.M. Power, Cubital tunnel syndrome, EFORT Open Rev 6 (2021) 743–750, https://doi.org/10.1302/2058-5241.6.200129.

[9] J. Zhang, Y. Chen, Y. Huang, W. Wu, X. Deng, H. Liu, R. Li, J. Tao, X. Li, X. Liu, M. Gou, A 3D-printed self-adhesive bandage with drug release for peripheral nerve repair, Adv. Sci. 7 (2020) 1–10, https://doi.org/10.1002/advs.202002601.

[10] X. Zhang, W. Qu, D. Li, K. Shi, R. Li, Y. Han, E. Jin, J. Ding, X. Chen, Functional polymer-based nerve guide conduits to promote peripheral nerve regeneration, Adv. Mater. Interfac. 7 (2020) 1–21, https://doi.org/10.1002/admi.202000225.

[11] A. Baron, A. Strohl, Severe cubital tunnel syndrome: considerations for nerve transfer surgery, Curr. Rev. Musculoskelet. Med. 13 (2020) 708–716, https://doi.org/10.1007/s12178-020-09676-2.

[12] T.A. Prest, E. Yeager, S.T. LoPresti, E. Zygelyte, M.J. Martin, L. Dong, A. Gibson, O. O. Olutoye, B.N. Brown, J. Cheetham, Nerve-specific, xenogeneic extracellular matrix hydrogel promotes recovery following peripheral nerve injury, J. Biomed. Mater. Res. A. 106 (2018) 450–459, https://doi.org/10.1002/jbm.a.36235.

[13] B. Zhao, Q. Zhang, X. Liang, J. Xie, Q. Sun, Quercetin reduces inflammation in a rat model of diabetic peripheral neuropathy by regulating the TLR4/MyD88/NF-κB signalling pathway, Eur. J. Pharmacol. 912 (2021), 174607, https://doi.org/10.1016/j.ejphar.2021.174607.

[14] B. Fan, M. Chopp, Z.G. Zhang, X.S. Liu, Treatment of diabetic peripheral neuropathy with engineered mesenchymal stromal cell-derived exosomes enriched with microRNA-146a provide amplified therapeutic efficacy, Exp. Neurol. 341 (2021), 113694, https://doi.org/10.1016/j.expneurol.2021.113694.

[15] Y. Luo, L. Fan, C. Liu, H. Wen, S. Wang, P. Guan, D. Chen, C. Ning, L. Zhou, G. Tan, An injectable, self-healing, electroconductive extracellular matrix-based hydrogel for enhancing tissue repair after traumatic spinal cord injury, Bioact. Mater. 7 (2022) 98–111, https://doi.org/10.1016/j.bioactmat.2021.05.039.

[16] L. Zhou, L. Fan, X. Yi, Z. Zhou, C. Liu, R. Fu, C. Dai, Z. Wang, X. Chen, P. Yu, D. Chen, G. Tan, Q. Wang, C. Ning, Soft conducting polymer hydrogels cross-linked and doped by tannic acid for spinal cord injury repair, ACS Nano 12 (2018) 10957–10967, https://doi.org/10.1021/acsnano.8b04609.

[17] L. Fan, C. Liu, X. Chen, L. Zheng, Y. Zou, H. Wen, P. Guan, F. Lu, Y. Luo, G. Tan, P. Yu, D. Chen, C. Deng, Y. Sun, L. Zhou, C. Ning, Exosomes-loaded electroconductive hydrogel synergistically promotes tissue repair after spinal cord injury via immunoregulation and enhancement of myelinated axon growth, Adv. Sci. 9 (2022) 1–22, https://doi.org/10.1002/advs.202105586.

[18] Y. Qian, Y. Cheng, J. Song, Y. Xu, W.-E. Yuan, C. Fan, X. Zheng, Mechano-informed biomimetic polymer scaffolds by incorporating self-powered zinc oxide nanogenerators enhance motor recovery and neural function, Small 16 (2020), e2000796, https://doi.org/10.1002/smll.202000796.

[19] J.M. Nichols, C.V. Crelli, L. Liu, H.V. Pham, J.M. Janjic, A.J. Shepherd, Tracking macrophages in diabetic neuropathy with two-color nanoemulsions for near-infrared fluorescent imaging and microscopy, J. Neuroinflammation 18 (2021) 1–22, https://doi.org/10.1186/s12974-021-02365-y.

[20] L.W. Chu, K.I. Cheng, J.Y. Chen, Y.C. Cheng, Y.C. Chang, J.L. Yeh, J.H. Hsu, Z. K. Dai, B.N. Wu, Loganin prevents chronic constriction injury-provoked neuropathic pain by reducing TNF-α/IL-1β-mediated NF-κB activation and Schwann cell demyelination, Phytomedicine 67 (2020), 153166, https://doi.org/10.1016/j.phymed.2019.153166.

[21] W.L. Dai, B. Yan, Y.N. Bao, J.F. Fan, J.H. Liu, Suppression of peripheral NGF attenuates neuropathic pain induced by chronic constriction injury through the TAK1-MAPK/NF-κB signaling pathways, Cell Commun. Signal. 18 (2020) 1–13, https://doi.org/10.1186/s12964-020-00556-3.

[22] T. Xue, X. Zhang, Y. Xing, S. Liu, L. Zhang, X. Wang, M. Yu, Advances about immunoinflammatory pathogenesis and treatment in diabetic peripheral neuropathy, Front. Pharmacol. 12 (2021) 1–10, https://doi.org/10.3389/fphar.2021.748193.

[23] Q. Wei, Y. Su, H. Xin, L. Zhang, J. Ding, X. Chen, Immunologically effective biomaterials, ACS Appl. Mater. Interfaces 13 (2021) 56719–56724, https://doi.org/10.1021/acsami.1c14781.

[24] Z. Zhong, A. Chen, Z. Fa, Z. Ding, L. Xiao, G. Wu, Q. Wang, R. Zhang, Bone marrow mesenchymal stem cells upregulate PI3K/AKT pathway and down-regulate NF-κB pathway by secreting glial cell-derived neurotrophic factors to regulate microglial polarization and alleviate deafferentation pain in rats, Neurobiol. Dis. 143 (2020), 104945, https://doi.org/10.1016/j.nbd.2020.104945.

[25] Y. Huh, R.R. Ji, G. Chen, Neuroinflammation, bone marrow stem cells, and chronic pain, Front. Immunol. 8 (2017), https://doi.org/10.3389/fimmu.2017.01014.

[26] L. He, T. He, J. Xing, Q. Zhou, L. Fan, C. Liu, Y. Chen, D. Wu, Z. Tian, B. Liu, L. Rong, Bone marrow mesenchymal stem cell-derived exosomes protect cartilage damage and relieve knee osteoarthritis pain in a rat model of osteoarthritis, Stem Cell Res. Ther. 11 (2020) 1–15, https://doi.org/10.1186/s13287-020-01781-w.

[27] L. Fan, P. Guan, C. Xiao, H. Wen, Q. Wang, C. Liu, Y. Luo, L. Ma, G. Tan, P. Yu, L. Zhou, C. Ning, Exosome-functionalized polyetheretherketone-based implant with immunomodulatory property for enhancing osseointegration, Bioact. Mater. 6 (2021) 2754–2766, https://doi.org/10.1016/j.bioactmat.2021.02.005.

[28] P. Guan, C. Liu, D. Xie, S. Mao, Y. Ji, Y. Lin, Z. Chen, Q. Wang, L. Fan, Y. Sun, Exosome-loaded extracellular matrix-mimic hydrogel with anti-inflammatory property Facilitates/promotes growth plate injury repair, Bioact. Mater. 10 (2022) 145–158, https://doi.org/10.1016/j.bioactmat.2021.09.010.

[29] Q. Li, H. Yu, M. Sun, P. Yang, X. Hu, Y. Ao, J. Cheng, The tissue origin effect of extracellular vesicles on cartilage and bone regeneration, Acta Biomater. 125 (2021) 253–266, https://doi.org/10.1016/j.actbio.2021.02.039.

[30] R. Sun, S. Xu, Z. Wang, Rat sinus mucosa- and periosteum-derived exosomes accelerate osteogenesis, J. Cell. Physiol. 234 (2019) 21947–21961, https://doi.org/10.1002/jcp.28758.

[31] L. Bonjoch, V. Casas, M. Carrascal, D. Closa, Involvement of exosomes in lung inflammation associated with experimental acute pancreatitis, J. Pathol. 240 (2016) 235–245, https://doi.org/10.1002/path.4771.

[32] S. Zhao, W. Li, W. Yu, T. Rao, H. Li, Y. Ruan, R. Yuan, C. Li, J. Ning, S. Li, W. Chen, F. Cheng, X. Zhou, Exosomal miR-21 from tubular cells contributes to renal fibrosis by activating fibroblasts via targeting PTEN in obstructed kidneys, Theranostics 11 (2021) 8660–8673, https://doi.org/10.7150/thno.62820.

[33] F.X. Zhang, P. Liu, W. Ding, Q.B. Meng, D.H. Su, Q.C. Zhang, R.X. Lian, B.Q. Yu, M. D. Zhao, J. Dong, Y.L. Li, L.B. Jiang, Injectable Mussel-Inspired highly adhesive hydrogel with exosomes for endogenous cell recruitment and cartilage defect regeneration, Biomaterials 278 (2021), 121169, https://doi.org/10.1016/j.biomaterials.2021.121169.

[34] L. Chen, Z. Chen, Z. Xu, W. Feng, X. Yang, Z. Qi, Polydatin protects Schwann cells from methylglyoxal induced cytotoxicity and promotes crushed sciatic nerves regeneration of diabetic rats, Phyther. Res. 35 (2021) 4592–4604, https://doi.org/10.1002/ptr.7177.

[35] T.L. Lopez-Silva, C.D. Cristobal, C.S. Edwin Lai, V. Leyva-Aranda, H.K. Lee, J. D. Hartgerink, Self-assembling multidomain peptide hydrogels accelerate peripheral nerve regeneration after crush injury, Biomaterials 265 (2021), 120401, https://doi.org/10.1016/j.biomaterials.2020.120401.

[36] M. Khanal, S.V. Gohil, E. Kuyinu, H.M. Kan, B.E. Knight, K.M. Baumbauer, K.W. H. Lo, J. Walker, C.T. Laurencin, L.S. Nair, Injectable nanocomposite analgesic delivery system for musculoskeletal pain management, Acta Biomater. 74 (2018) 280–290, https://doi.org/10.1016/j.actbio.2018.05.038.

[37] H.M. Guo, Y. Zhang, Y. Zhang, P.F. Jiao, X.C. Fan, C.L. Kong, T. Wang, X.X. Li, H. W. Zhang, L.R. Zhang, M.Y. Ma, H.L. Bu, Spinal Ninjurin2 contributes to the neuropathic pain via NF-κB-mediated neuroinflammation in the spared sciatic nerve injury rats, Int. Immunopharm. 99 (2021), 107918, https://doi.org/10.1016/j.intimp.2021.107918.

[38] N.M. Elsherbiny, E. Ahmed, G.A. Kader, Y. Abdel-mottaleb, M.H. ElSayed, A. M. Youssef, S.A. Zaitone, Inhibitory effect of valproate sodium on pain behavior in diabetic mice involves suppression of spinal histone deacetylase 1 and inflammatory mediators, Int. Immunopharm. 70 (2019) 16–27, https://doi.org/10.1016/j.intimp.2019.01.050.

[39] T. Suto, H. Obata, M. Tobe, H. Oku, H. Yokoo, Y. Nakazato, S. Saito, Long-term effect of epidural injection with sustained-release lidocaine particles in a rat model of postoperative pain, Br. J. Anaesth. 109 (2012) 957–967, https://doi.org/10.1093/bja/aes302.

[40] X. Gao, P. Zhu, L. Yu, L. Yang, Y. Chen, Ultrasound/acidity-triggered and nanoparticle-enabled analgesia, Adv. Healthc. Mater. 8 (2019) 1–10, https://doi.org/10.1002/adhm.201801350.

[41] X. Zhao, C. Fan, J. Wang, H. Xiong, T. Zhu, Y. Liu, H. Pan, W. Weijia Lu, Bioinspired multichannel nerve guidance conduit based on shape memory nanofibers for potential application in peripheral nerve repair, ACS Nano 14 (2020) 12579–12595, https://doi.org/10.1021/acsnano.0c03570.

[42] L. Fan, C. Xiao, P. Guan, Y. Zou, H. Wen, C. Liu, Y. Luo, G. Tan, Q. Wang, Y. Li, P. Yu, L. Zhou, C. Ning, Extracellular matrix-based conductive interpenetrating network hydrogels with enhanced neurovascular regeneration properties for diabetic wounds repair, Adv. Healthc. Mater. 11 (2022), e2101556, https://doi.org/10.1002/adhm.202101556.

[43] N.P. Gonçalves, C.B. Vægter, H. Andersen, L. Østergaard, N.A. Calcutt, T.S. Jensen, Schwann cell interactions with axons and microvessels in diabetic neuropathy, Nat. Rev. Neurol. 13 (2017) 135–147, https://doi.org/10.1038/nrneurol.2016.201.

[44] R. Li, K. Liu, X. Huang, D. Li, J. Ding, B. Liu, X. Chen, Bioactive materials promote wound healing through modulation of cell behaviors, Adv. Sci. 9 (2022) 1–22, https://doi.org/10.1002/advs.202105152.

[45] Z. Chen, A. Bachhuka, S. Han, F. Wei, S. Lu, R.M. Visalakshan, K. Vasilev, Y. Xiao, Tuning chemistry and topography of nanoengineered surfaces to manipulate immune response for bone regeneration applications, ACS Nano 11 (2017) 4494–4506, https://doi.org/10.1021/acsnano.6b07808.

[46] G. Sun, G. Li, D. Li, W. Huang, R. Zhang, H. Zhang, Y. Duan, B. Wang, hucMSC derived exosomes promote functional recovery in spinal cord injury mice via attenuating inflammation, Mater. Sci. Eng. C 89 (2018) 194–204, https://doi.org/10.1016/j.msec.2018.04.006.

[47] M. Ghibaudi, M. Boido, A. Vercelli, Functional integration of complex miRNA networks in central and peripheral lesion and axonal regeneration, Prog. Neurobiol. 158 (2017) 69–93, https://doi.org/10.1016/j.pneurobio.2017.07.005.

[48] H. Xin, Z. Liu, B. Buller, Y. Li, W. Golembieski, X. Gan, F. Wang, M. Lu, M.M. Ali, Z. G. Zhang, M. Chopp, MiR-17-92 enriched exosomes derived from multipotent mesenchymal stromal cells enhance axon-myelin remodeling and motor electrophysiological recovery after stroke, J. Cerebr. Blood Flow Metabol. 41 (2021) 1131–1144, https://doi.org/10.1177/0271678X20950489.

[49] T.D. Glenn, W.S. Talbot, Signals regulating myelination in peripheral nerves and the Schwann cell response to injury, Curr. Opin. Neurobiol. 23 (2013) 1041–1048, https://doi.org/10.1016/j.conb.2013.06.010.

[50] M.B. Christensen, P.A. Tresco, Differences exist in the left and right sciatic nerves of naïve rats and cats, Anat. Rec. 298 (2015) 1492–1501, https://doi.org/10.1002/ar.23161.